JOURNAL OF GEOPHYSICAL RESEARCH, VOL. 112, B06307, doi:10.1029/2006JB004615, 2007

Strong ground motion simulation of the 1999 Chi-Chi, Taiwan earthquake from a realistic three-dimensional source and crustal structure

Shiann-Jong Lee,[1] How-Wei Chen,[2] and Kuo-Fong Ma[2]

Received 5 July 2006; revised 2 February 2007; accepted 26 March 2007; published 21 June 2007.

[1] We simulate the strong ground motion of 1999 Chi-Chi, Taiwan earthquake (M_w = 7.6) by considering a three-dimensional source rupture model in a full waveform three-dimensional wave propagation study. The strong ground motion records during the 1999 Chi-Chi earthquake show various characteristics at different sites in Taiwan. We adopt a three-dimensional source model derived from an inversion study with identical path effects as considered in this three-dimensional forward study. Comparisons between the simulation results and observed waveforms from dense island-wide strong motion stations demonstrate that the fault geometry, lateral velocity variation, and complex source rupture process greatly influence the distribution of strong ground shaking. The simulation has reproduced the heavy damage area that is mainly concentrated in the hanging wall, especially close to the surface break of the Chelungpu fault. The source directivity effect is also reproduced and shows serious shaking along the northward rupture direction. Low-velocity material in the shallow part of the Western Plain is found to generate significantly amplified ground motions. In the Central Range, the shaking is relatively weak owing to the energy radiation characteristics of a low-angle thrust of the Chelungpu faulting system. The wavefield is then amplified by a high-velocity gradient under the Coastal Range. Our simulation results in the frequency range of 0.01–0.5 Hz give good agreement with the extensive strong motion observations of the Chi-Chi earthquake. We find that adequate source representation, good three-dimensional crustal velocity structures, and careful numerical work are necessary to make the ground motion prediction feasible.

Citation: Lee, S.-J., H.-W. Chen, and K.-F. Ma (2007), Strong ground motion simulation of the 1999 Chi-Chi, Taiwan earthquake from a realistic three-dimensional source and crustal structure, *J. Geophys. Res.*, *112*, B06307, doi:10.1029/2006JB004615.

1. Introduction

[2] The source process and strong ground motion are two important topics in seismology as they are necessary for seismic hazard mitigation. High-resolution source inversion and three-dimensional wave propagation simulations are keys in solving problems of strong motion prediction. Although the 1999 Chi-Chi earthquake ± M_w = 7.6) has inflicted a loss of life and economic damage in Taiwan, it nonetheless has provided one of the best data sets used to investigate many fundamental problems of a complex source rupture and wave propagation in a heterogeneous crust. At the same time, it offers an excellent opportunity to calibrate our tools against real data for strong motion prediction.

[3] Over the past 5 years, a good number of studies have been published on the source inversion of the Chi-Chi earthquake. Each of these studies has addressed certain specific aspects of the source rupture process: several papers deal with the source geometry and rupture dynamics [*Ma et al*, 2001; *Zeng and Chen*, 2001; *Wu et al.*, 2001], a few papers examine the influence of the velocity field [*Cheng*, 2000; *Chen et al.*, 2001], and a paper looks into the response of local site effect during the earthquake [*Furumura et al.*, 2001]. A reasonably accurate description of the physics of the rupture process has been derived from these studies. However, each study is by-and-large focused on certain aspects of the overall process: for example, some pay more attention to the source rupture, others on the path influence, and one on the station site complexity. When concentrating on some aspects, other aspects are generally treated as known quantities with accompanying simplified assumptions. For example, in an inversion process of a source rupture, the path effect is usually assumed as a one-dimensional velocity structure, found in the 1983 Imperial Valley, California earthquake [*Hartzell and Heaton*, 1983], the 1992 Landers, California earthquake [*Wald and Heaton*, 1994], and the 1999 Chi-Chi, Taiwan earthquake [*Ma et al.*, 2001], while in reality, the source process and path effects

[1]Institute of Earth Sciences, Academia Sinica, Taiwan.
[2]Institute of Geophysics, National Central University, Taiwan.

0148-0227/07/2006JB004615$09.00

are closely coupled with a high degree of complexity. This complex coupling has been examined for some large earthquakes. *Furumura and Koketsu* [2000] combine a source model from the work of *Yoshida et al.* [1996] and a three-dimensional velocity model from the work of *Kagawa et al.* [1993] to perform forward modeling of the strong ground motion along the surface break of the 1995 Kobe earthquake. *Furumura and Singh* [2002] used a similar scheme to combine the source model from the work of *Yagi and Kikuchi* [2000] to analyze the strong motion process during the Chi-Chi earthquake. From these results, we have gained some understanding of the relation between the source processes of large earthquakes and induced strong motions. However, the path effect is still not adequately modeled in many source inversion results and forward wave propagation studies. In order to further understand the influence of source, path, and even site effects on observations, it is necessary to take into account the complexities of both source rupture and three-dimensional structure at the same time.

[4] The goal of this study is to make a realistic three-dimensional forward calculation of the strong motion field on the basis of the source model obtained from an inversion in an earlier study [*Lee et al.*, 2006b]. This study takes advantage of the rich strong motion recordings of the Ch-Chi event and uses the waveform data to calibrate the results of forward simulation. The velocity model used in the previous inversion study and in this forward study is identical, a three-dimensional crustal structure derived from a travel-time tomography study by *Rau and Wu* [1995]. We will demonstrate with an adequate source model, reasonable three-dimensional crustal structure, and good numerical codes that simulated waveforms can indeed approximate the observed records reasonably well for the purpose of strong motion prediction.

2. Data and Method

2.1. Taiwan Strong-Motion Instrumentation Program Observations

[5] Instruments of the Central Weather Bureau's (CWB) Taiwan Strong-Motion Instrumentation Program (TSMIP), implemented in the early 1990s, have recorded an extensive set of strong motion data for both the main shock and many large aftershocks with the occurrence of the Chi-Chi earthquake sequence. For the main shock, 441 sets of digital strong motion records were obtained and processed from a total of 663 triggered data files. This data set is important for both seismology and earthquake engineering because it includes over 60 recording sites within 20 km of the fault ruptures, which provides a fivefold increase in such near-field records available for the entire world to that date. Strong motion records for this earthquake are highly valuable because of the nearly complete coverage they have provided of the large (M_w7.6) event of long (100 km) surface rupture. The ground acceleration for the stations at the southern part of the fault is quite large. Most of the near-field stations record the peak ground acceleration near 1*g*, such as TCU129 (Figure 1a). However, larger ground velocity and large displacement are measured at the northern part of the fault, for example, TCU052 and TCU068, where largest surface breaks are observed. On the hanging wall, both the peak ground acceleration (PGA) and peak ground velocity (PGV) are extremely large with some of the records having a PGA of over 1*g* (TCU084). Although the ground shaking was relatively small on the footwall, long-period surface wave-like phases also caused serious damage [*Chang et al.*, 2002] in cities built over the sedimentary plains. Another notable phenomenon for this earthquake is that the PGV is generally higher at the northern area of the source region. A large PGV extends over most of the northwest Taiwan. This, as we will see from our numerical simulation, clearly reflects the northward rupture source directivity. Furthermore, some places far from the epicenter, such as the Taipei metropolitan area, Ilan plain, and along the Longitudinal Valley, have developed notable ground motion amplifications. The complex distribution of strong motion observations, as will be seen from results of our numerical simulations, is an expected convolution of a large propagating rupture with an equally complex crustal structure with sedimentary plains and valleys.

2.2. Three-Dimensional Source Rupture Model

[6] The study of spatial-temporal slip distributions of the 1999 Chi-Chi earthquake has been carried out by many researchers in recent years [*Lee and Ma*, 2000; *Ma et al.*, 2001; *Zeng and Chen*, 2001; *Wu et al.*, 2001; *Ji et al.*, 2001], revealing a general consistency of resulting source rupture models derived from the inversion using teleseismic broadband data near-field strong motion data, Global Positioning System (GPS) data, and surface rupture data. However, some fault models used in these inversion studies were based on a simplified fault geometry that had been shown not to be consistent with near-field data [*Lee et al.*, 2006a]. In addition, all Green's functions calculated for these inversions were derived from a one-dimensional or modified one-dimensional layered velocity model which can hardly explain the lateral wave propagation properties in Taiwan. This has an important impact on the estimation of the path effects.

[7] Using a recently developed three-dimensional velocity model [*Rau and Wu*, 1995], we adopt the source inversion result from the work of *Lee et al.* [2006b] (Figure 1b) in the current forward simulation calculations. Several efforts had been made in the paper of *Lee et al.* [2006a, 2006b] to refine the source model for simulation of higher resolution three-dimensional rupture process. These include (1) dense near-field strong motion data which provided about a fivefold increase in the source region records available for the entire world; (2) using a three-dimensional trend-surface as the fault model to approximate recently revealed fault geometry; (3) comprehensive three-dimensional Green's functions, which were calculated to satisfy the complex three-dimensional velocity and improve the accuracy of source simulation; and (4) taking into account the absolute timing for both Green's functions and observations. For the three-dimensional fault model, the geometry is established by surface fault trace and 327 relocated aftershocks by means of trend surface analysis [*Lee et al.*, 2006a]. We give each subfault with a length and downdip width of 3 km in a finite-fault approach. The total number of subfaults in the three-dimensional trend surface fault model is 357. We perform the inversion under a parallel environment utilizing

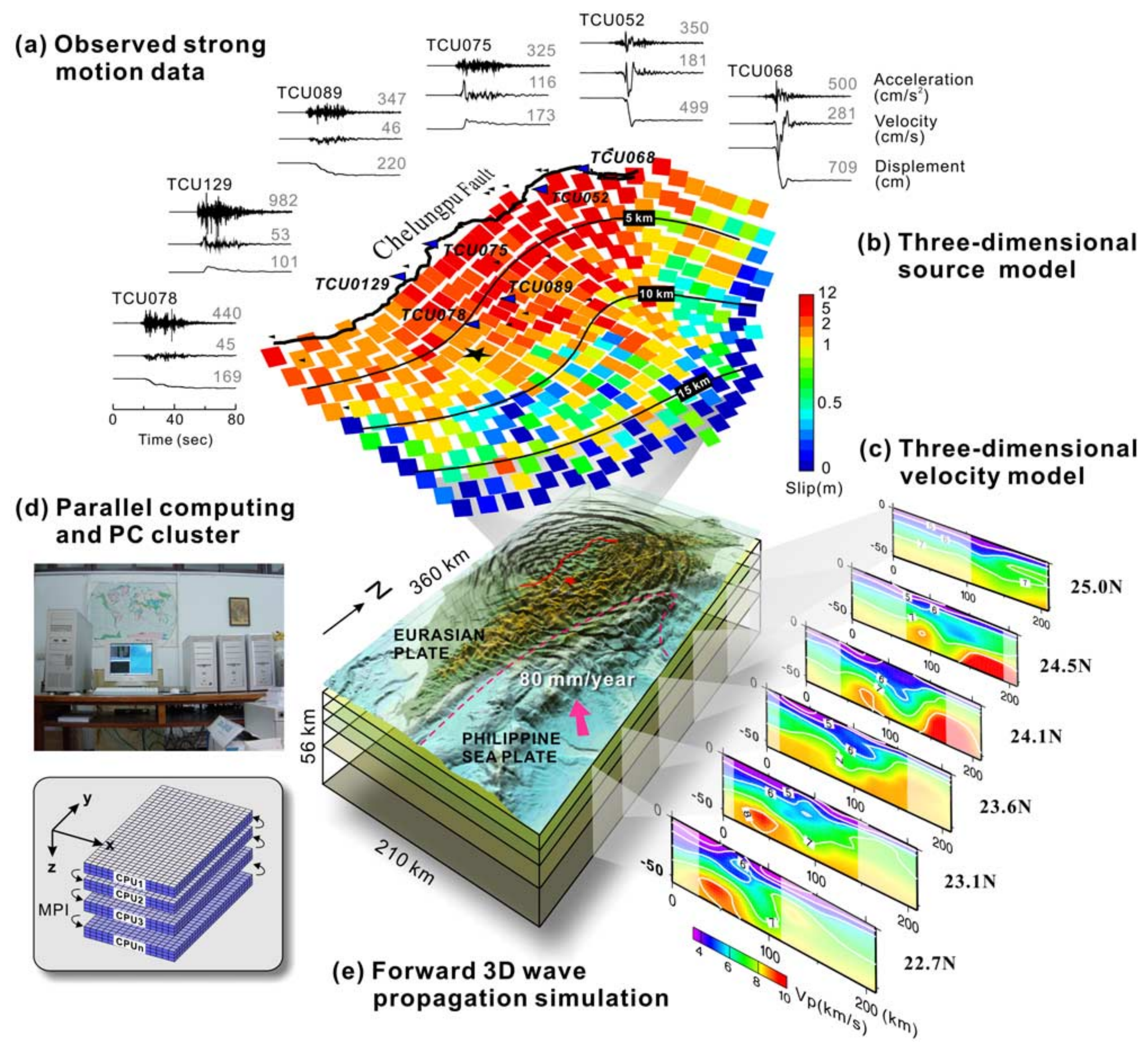

Figure 1. Three-dimensional ground motion simulation framework of the 1999 Chi-Chi, Taiwan earthquake. (a) The near-field strong motion records. Labels at the end of the waveforms indicate the maximum acceleration (cm/s^2), velocity (cm/s), and displacement (cm), respectively. (b) The three-dimensional rupture process model from the source inversion study by *Lee et al.* [2006b]. (c) The three-dimensional velocity model used in the study derived from a travel-time tomography inversion [*Rau and Wu*, 1995]. (d) A parallel computing technique is applied by using a PC cluster in this simulation. The model is decomposed with respect to depth, and the message passing interface (MPI) is used to communicate the information between computing nodes. (e) The forward ground motion simulation derives from a realistic source process and three-dimensional crustal structure. By combining most of the recently available near-field ground motion records and earthquake source information, this comprehensive study successfully reproduced major properties of strong ground shaking during the 1999 Chi-Chi earthquake.

multiple-time window to manage the large data volume and source parameters. This allowed each subfault to slip in any one of 2.0-s time windows following the passage of the rupture front. Under the multiple-time window condition, the source time function and rupture velocity in the inversion could be more flexible and resulting in more reliable source rupture model.

[8] The refinements show that the Chi-Chi earthquake has a highly complex spatiotemporal rupture behavior with a major slip area located at shallow part of the fault above the decollement about 10 km from the surface. The decollement structure was well constrained by the three-dimensional fault geometry, which had a gentle dip and becomes even gentler in the deeper part. Two large

asperities arise during the rupture process: one at the middle part of the fault near the TsaoTun area; the other located near the northern bending of the fault where largest slip (about 15 m) occurred. The slip behavior on the Chelungpu fault rupture is heterogeneous. In the southern part, a small rupture repeats several times, while in the northern part, there is only one major large rupture with a duration time of about 10 s. Another important point adopted in this source model is that the Green's function used in the inversion is calculated by the same finite difference method with the identical three-dimensional velocity model used in this study and follow the same path effect during the study. The detail descriptions of the results of three-dimensional source process inversion have been given in the paper of *Lee et al.* [2006b].

2.3. Simulation Method and Model Setting

[9] A modified elastic finite difference code [*Chang and McMechan*, 1987, 1994] for three-dimensional wavefield simulation is used in predicting ground motion. Although the proposed algorithm for earthquake source imaging was published [*Chang and McMechan*, 1991], the field data implementation is still limited by the computational resource and the amount of data available. The in-house developed numerical program is further modified to incorporate more realistic double-couple source characterization and with more effective absorbing condition. Detail comparison of numerical accuracy and stability against the community reference models of Southern California Earthquake Center (SCEC) was performed to ensure that the calculation is consistent to within acceptable accuracy. Some minor differences may attribute to the details in creating numerical model, discrete grid spacing, source, and numerical implementation of three-dimensional time domain elastic finite difference wave equations. The numerical accuracy and stability were further tested considering regular- versus staggered-grid computation [*Chen*, 1996], explicit versus implicit scheme, and the order of derivative approximation both in space and time. Attention is paid to the influence of lateral wave propagation, and anelasticity is temporarily ignored. The three-dimensional velocity model for the whole Taiwan used in our study is derived from traveltime tomography inversion results by *Rau and Wu* [1995]. The estimated three-dimensional velocity model has its nature of smoothness and long-wavelength characteristics in lateral variation of elastic wave speed. Figure 1c shows several velocity profiles in the west-east direction across Taiwan. The relationship between the main tectonic settings and three-dimensional velocity characteristics in Taiwan region is illustrated. The velocity at the shallow part of western Taiwan is relatively slow, which reflects the deep sedimentary material under the Western Plain. In the east part, high-velocity material is found near the surface because of the collision of the Philippine Sea Plate. Furthermore, the isovelocity line at the depth of 7 km/s varies from south to north, which represents the nature of different mountain-building periods. We can also find a wedge-shaped velocity pattern at the shallow part of western Taiwan that is corresponding to the thin-skinned model as described by *Suppe* [1980a, 1980b] and *Wang et al.* [2000]. *Lee and Chen* [2000] have found that this tomography model provides more evident three-dimensional traveltime characteristics than other tomography inversion results [*Ma et al.*, 1996].

[10] Considering the best available tomography velocity model derived from the data collected by the CWB network with relatively large interstation spacing of 30 km and computation time required for Chi-Chi earthquake source inversion and forward studies, the trade-off between efficiency, in-core computation, and accuracy have to be carefully evaluated. For a fairly large-scale (335 km $\times$ 210 km $\times$ 56 km) and lower-frequency (0.01–0.5 Hz) response simulation in our study, a composite boundary condition, including the A_2 boundary condition [*Clayton and Engquist*, 1977] and nonreflecting boundary condition [*Cerjan et al.*, 1985; *Chang and McMechan*, 1989], is used to effectively avoid the artificial reflections from the model boundary. The velocity model is then divided into 0.5-km grids. With this resolution, a total of 36.2 million grid points are needed for the whole Taiwan crustal structure. With limited velocity-model resolution and computational resources in mind, the second-order finite difference method is considered as an effective scheme for three-dimensional wave propagation except that the grid spacing has to be sufficiently small in achieving acceptable accuracy. Furthermore, in large-scale three-dimensional simulation, the full waveform calculation is complex and time consuming for a simple workstation environment. Thus parallel computing with a personal computer (PC) cluster is used in this study. We used the message-passing interface (also known as MPI, *Gropp et al.* [1996]) to separate the calculation into numerous computing nodes with respect to the depth (Figure 1d). Three component wavefields and the velocity model are then decomposed and calculated in the individual computing node. By this approach, not only the memory capacity problem for large-scale simulation can be solved, but the computing time can be reduced effectively. Considering the number of grid points per wavelength for stable computation, the resolution involved in choosing the interpolation scheme in constructing three-dimensional velocity model and the limitation of our computing capacity, frequency content of the synthetic Green's function, is restricted to be under 0.5 Hz.

[11] We use the moment tensor representation for the complex energy radiation at different parts of the fault rupture surface, which is subdivided into 357 subfaults. Nine moment tensor densities are set around the central point on each subfault. For different focal mechanism, we define the radiation characteristics of the double couple source, each giving nine moment tensor densities with different weighting. From the Chi-Chi earthquake source inversion result of a rupture duration of 60 s [*Lee et al.*, 2006b], we put all 21,420 point sources in the model with appropriate locations, timing, and energy radiate properties to reproduce the overall complex rupture process of the Chi-Chi earthquake. Because of the domain decomposition in parallel computing, the excitation of these point sources needs to be carefully defined. We set up these sources according to the depth into different computing nodes. MPI is then used to exchange the wavefield information between boundaries in different nodes. By the parallelization of the source excitation process, the whole three-dimensional energy radiation characteristics during the Chi-Chi earthquake can be well defined, and possible

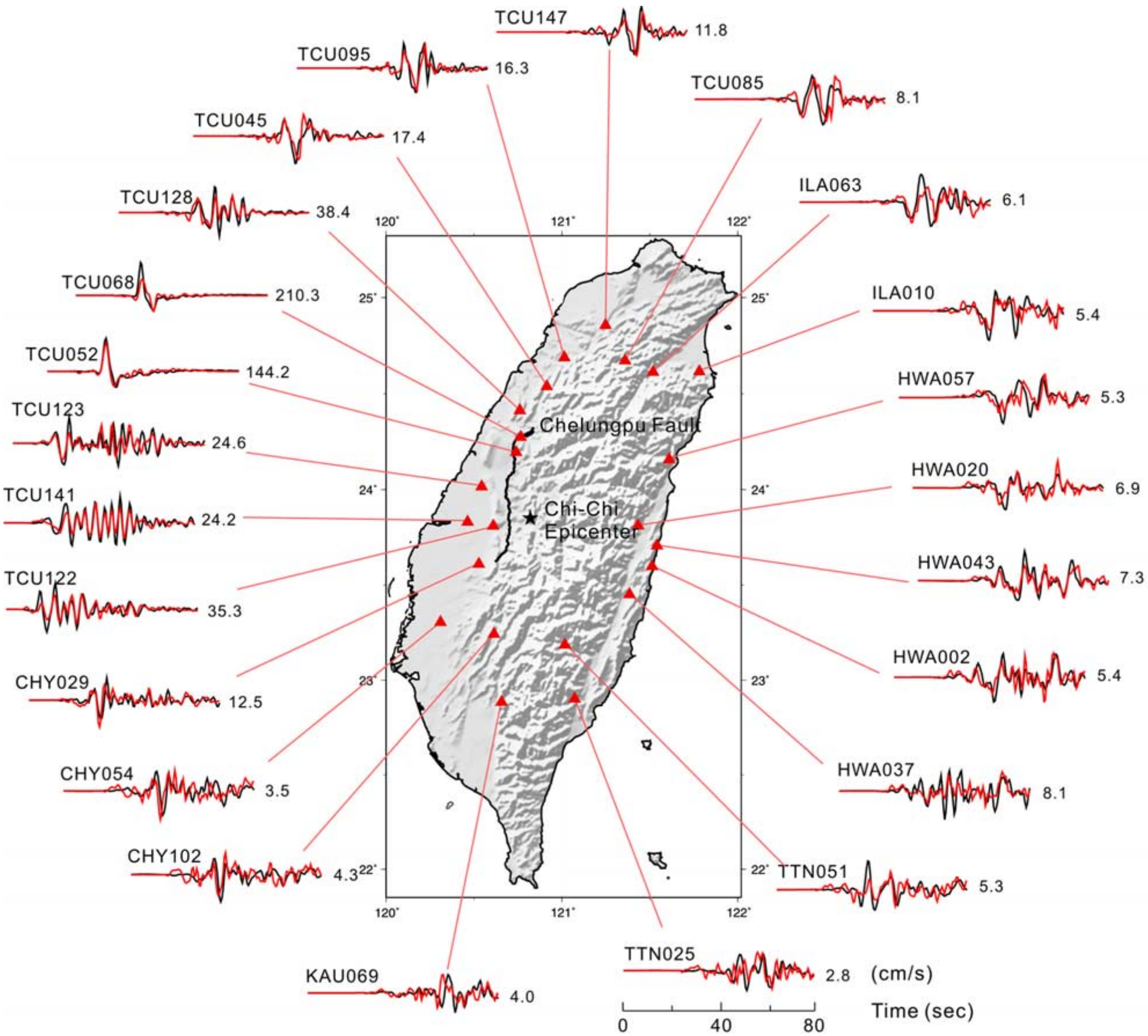

Figure 2. Comparison between observed and synthetic waveforms. (a) Stations used in the inversion. The synthetic waveforms are represented by red lines; (b) stations not been used in the inversion. The synthetic waveforms are shown by blue lines. At the end of the seismograms are the labels of peak ground-velocity values in the records. The Chi-Chi earthquake epicenter (star) and Chelungpu fault surface break (bold line) are shown in the figure. The open square in Figure 2b indicates the Taipei basin area.

interactions between ground motions and source rupture process can be examined.

3. Forward Simulation Result

3.1. Observation Versus Synthetic

[12] The forward simulation of velocity waveforms are examined by comparing actual observed waveforms. Figure 2 shows part of the stations analyzed in the study and their corresponding seismograms. All the stations can be divided into two sets, set A and set B: A stations used in the previous inversion study (Figure 2a; Table 1) and B stations not used in the inversion (Figure 2b; Table 2). In order to increase the resolution by reducing complexity caused by the path effect, only the stations which have a shorter distance to the surface break were taken into account in the inversion study. Meanwhile almost all near-field records were used to have better azimuth coverage around the source area. Totally, 103 three-component set A stations, with a total of 309 records, are taken in the source inversion to obtain the highest resolution [*Lee et al.*, 2006b].

[13] We examined the forward simulation result of set A stations first (Figure 2a). Because the same three-dimensional velocity model is used in both the inversion and forward simulation, we expect that the forward simulation waveforms are in excellent agreement with set A. Stations at the northern part of the Chelungpu fault (for example, TCU052, TCU68, and TCU128) show simpler waveforms while having the largest amplitude

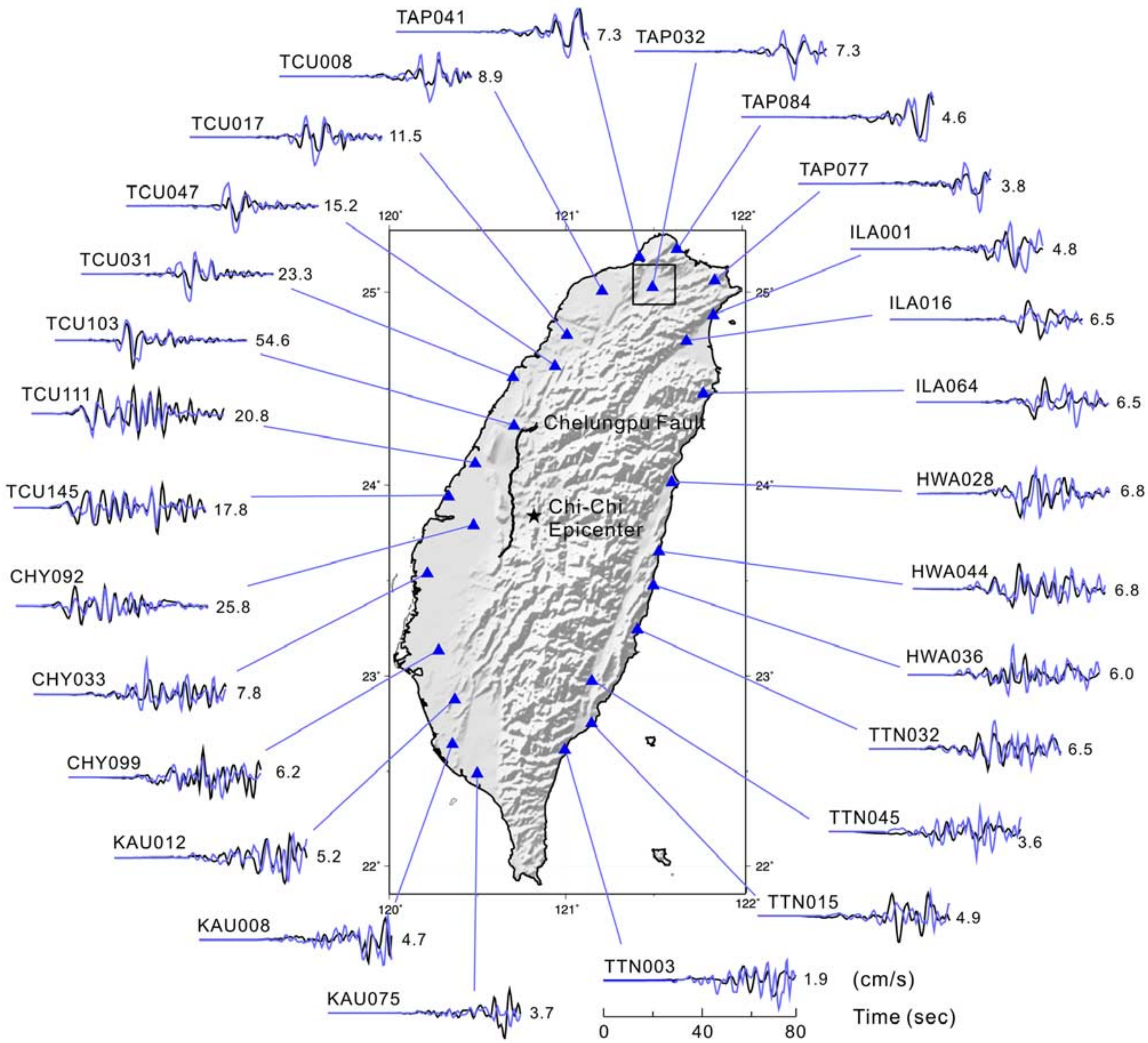

Figure 2. (continued)

of ground velocity. Our synthetics match most of these observed waveforms very well. At the footwall of the Chelungpu fault, for example, central-western Taiwan, most of the records show complex surface wave-like energy (such as TCU141); still, the synthetic waveforms can explain these phases sufficiently well. Around the southern part of the fault, both the synthetics and observations (for example, CHY054 and CHY102) show a main phase with smaller peak-velocity amplitude. In the eastern part of the fault, the synthetics give a reasonable fit in low-frequency phases for northern stations such as ILA010 and HWA057. However, the discrepancy is larger in southern stations which have more high frequency parts, for example, HWA037 and TTN025. This discrepancy is also found in the results of our previous inversion study.

[14] By using a three-dimensional rupture inversion result as the source model with identical path effects derived from a reasonably good three-dimensional crustal model, we have found that not only stations used in the inversion (set A) can have the precise fit as expected [*Lee et al.*, 2006b], but also stations not used in the inversion (set B) show a good fit in waveforms. Part of the forward simulation results of set B stations is shown in Figure 2b. Although most of the set B stations have larger distances to the surface break compared to set A stations, the synthetics still can explain the observed records. We represent our results by dividing set B stations into four parts: (1) Northern Taiwan, (2) Southern Taiwan, (3) Eastern Taiwan, and (4) Western Taiwan. (1) For the stations in north Taiwan where the rupture is directing, a specified characteristic resulted from the directivity effect of a long period, and large amplitude phase recorded in both set A and set B are explained well in the forward synthetic waveforms, such as TCU095 and TCU147 in set A and TCU017, TAP041, and TAP084 in set B. (2) Toward south Taiwan where the rupture is going away

Table 1. Set A Stations Which are Used in the Inversion Study

Station	Log	Lat	Epi	D_{rup}	PGA
CHY006	120.552	23.582	39.90	14.53	0.36
CHY008	120.269	23.485	68.20	45.23	0.13
CHY024	120.606	23.757	22.80	9.26	0.28
CHY025	120.514	23.780	30.50	18.78	0.17
CHY028	120.605	23.632	32.10	8.67	0.76
CHY029	120.528	23.614	38.90	16.40	0.29
CHY035	120.584	23.520	43.60	15.20	0.25
CHY041	120.596	23.439	51.10	21.94	0.64
CHY046	120.463	23.477	54.60	27.80	0.19
CHY054	120.310	23.308	79.00	51.68	0.10
CHY058	120.319	23.173	90.60	62.02	0.06
CHY063	120.340	23.027	103.50	74.41	0.07
CHY074	120.805	23.510	38.80	14.37	0.23
CHY076	120.222	23.638	47.70	51.49	0.07
CHY078	120.228	23.040	79.31	81.45	0.09
CHY080	120.678	23.597	2.47	4.93	0.86
CHY087	120.519	23.385	60.00	31.06	0.14
CHY094	120.321	23.794	49.40	38.54	0.06
CHY101	120.562	23.686	30.90	13.31	0.40
CHY102	120.614	23.246	41.86	42.41	0.05
HWA002	121.512	23.601	78.10	53.10	0.09
HWA019	121.605	23.977	83.00	54.47	0.14
HWA020	121.433	23.814	64.70	44.71	0.07
HWA024	121.297	23.352	38.66	43.80	0.03
HWA026	121.617	24.119	87.90	53.82	0.07
HWA027	121.591	24.055	83.40	51.67	0.12
HWA032	121.412	23.711	64.60	43.34	0.15
HWA033	121.475	23.687	71.50	49.18	0.17
HWA034	121.377	23.591	66.10	40.87	0.14
HWA035	121.436	23.732	66.40	45.41	0.08
HWA037	121.384	23.454	74.70	44.48	0.13
HWA038	121.345	23.462	71.00	40.99	0.06
HWA043	121.540	23.709	51.26	55.14	0.07
HWA045	121.741	24.310	107.80	65.20	0.19
HWA056	121.508	24.180	41.59	42.73	0.11
HWA057	121.610	24.160	88.90	53.01	0.12
HWA058	121.484	23.967	70.70	43.25	0.12
ILA010	121.781	24.619	130.40	76.77	0.06
ILA024	121.588	24.645	118.20	61.52	0.04
ILA051	121.667	24.721	72.27	72.88	0.08
ILA061	121.825	24.523	76.47	77.04	0.05
ILA062	121.793	24.468	71.75	72.36	0.08
ILA063	121.518	24.616	111.00	54.01	0.09
ILA067	121.373	24.440	86.70	31.96	0.20
KAU020	120.535	22.902	109.50	80.74	0.08
KAU050	120.757	23.163	77.40	50.29	0.04
KAU051	120.620	22.372	165.80	138.08	0.01
KAU054	120.713	23.278	65.10	37.59	0.09
KAU069	120.657	22.887	108.70	80.91	0.04
TCU026	121.075	24.776	105.20	50.98	0.12
TCU029	120.749	24.559	77.50	24.49	0.16
TCU033	120.862	24.686	91.60	39.60	0.19
TCU038	120.663	24.491	71.20	18.24	0.15
TCU039	120.784	24.492	70.00	17.52	0.20
TCU045	120.914	24.541	76.30	24.65	0.52
TCU046	120.854	24.468	67.60	16.48	0.14
TCU049	120.690	24.179	37.00	3.27	0.28
TCU052	120.739	24.198	37.90	1.84	0.45
TCU053	120.669	24.194	39.20	5.45	0.23
TCU054	120.675	24.161	35.70	4.64	0.19
TCU059	120.564	24.269	51.20	16.48	0.17
TCU060	120.644	24.225	43.30	8.12	0.20
TCU063	120.616	24.108	33.20	10.31	0.18
TCU064	120.610	24.346	57.10	12.24	0.12
TCU065	120.691	24.059	24.60	2.49	0.79
TCU067	120.720	24.091	26.80	1.11	0.50
TCU068	120.766	24.277	46.30	3.01	0.53
TCU070	120.540	24.196	45.60	18.43	0.25
TCU071	120.788	23.986	13.90	4.88	0.65
TCU072	120.849	24.041	20.60	7.87	0.47
TCU074	120.962	23.962	20.00	13.75	0.60
TCU075	120.678	23.983	18.40	3.38	0.33
TCU076	120.676	23.908	13.70	3.17	0.43
TCU078	120.846	23.812	7.10	8.27	0.45
TCU079	120.894	23.840	9.90	10.95	0.59
TCU084	120.900	23.883	10.50	11.40	1.01
TCU085	121.358	24.676	106.60	48.02	0.06
TCU087	120.773	24.348	54.10	3.42	0.12
TCU088	121.176	24.253	7.47	13.22	0.53
TCU089	120.857	23.904	7.50	8.33	0.35
TCU095	121.014	24.692	94.60	41.44	0.70
TCU102	120.721	24.249	43.80	1.19	0.30
TCU103	120.707	24.310	50.70	2.42	0.15
TCU109	120.571	24.085	34.00	14.69	0.16
TCU112	120.424	24.056	43.90	29.52	0.08
TCU116	120.580	23.857	22.30	12.46	0.19
TCU117	120.460	24.134	45.90	26.23	0.12
TCU120	120.613	23.980	23.20	9.87	0.23
TCU122	120.610	23.813	20.00	9.22	0.26
TCU123	120.544	24.019	31.40	17.11	0.15
TCU128	120.761	24.416	61.70	9.08	0.17
TCU129	120.684	23.878	11.90	2.21	1.00
TCU136	120.652	24.260	46.80	7.54	0.17
TCU140	120.359	23.958	46.10	35.54	0.07
TCU141	120.464	23.834	34.30	24.16	0.11
TCU147	121.248	24.859	119.60	62.10	0.13
TTN025	121.072	22.905	109.50	79.86	0.05
TTN031	121.460	23.356	87.50	55.39	0.09
TTN033	121.388	23.193	95.20	61.47	0.04
TTN041	121.118	23.134	52.41	56.38	0.08
TTN042	121.277	23.001	107.00	73.88	0.06
TTN044	121.166	23.007	101.70	70.26	0.06
TTN051	121.017	23.189	77.60	49.49	0.03

The columns from left to right are the station names of TSMIP, station longitude (Log) in degrees east, station latitude (Lat) in degrees north, distance (km) from the Chi-Chi epicenter (Epi), the closest distance (km) to the rupture surface (D_{rup}), and peak ground acceleration (PGA) in *G*.

from, the misfit between synthetics and observations is increased, i.e., CHY099 and KAU012. In this region, the source rupture effect is scattered; thus the local site effects begin to have apparent influence, which has not been precisely revealed in the three-dimensional velocity model derived from the traveltime tomography inversion. However, even though the observed waveforms are complex, the peak velocity values of the synthetics are comparable with these records. (3) Western Taiwan is located in the footwall of Chelungpu fault where waves move into sedimentary plain with variable site responses. However, because of a closer distance to the rupture area, the strong ground motion in this region is mainly dominated by an intense source effect which is well described by the source inversion study. The set B stations in this area, such as TCU111, TCU145, and CHY092, can have a good fit as in set A (for example, TCU122, TCU123, and TCU141). (4) Eastern Taiwan is the hanging wall where waves are crossing the central mountain range. Set B stations in this region are mostly located around the Longitudinal Valley and have more complex high-frequency waveforms. Because of the resolution of the three-dimensional velocity model and the limitation of the three-dimensional finite difference wave propagation code, the valley sediments and high mountain topography effect are not considered in our study model. In this case, some synthetics produce larger discrepancies in the records at these stations, such as HWA036 and TTN015.

[15] In sum, the set A and set B stations do not depart too much in west and east Taiwan, while in north and south

Table 2. Set B Stations Which are Not Used in the Inversion Study

Station	Log	Lat	Epi	D_{rup}	PGA
ALS	120.8052	23.5103	38.8	14.37	0.22
CHK	121.3653	23.0992	102.2	68.29	0.04
CHY	120.4245	23.4977	55.5	30.04	0.15
CHY002	120.4125	23.7192	42.4	28.74	0.14
CHY004	120.1715	23.6013	70.2	52.80	0.10
CHY010	120.5440	23.4653	50.9	22.40	0.23
CHY012	120.1523	23.3328	88.2	63.15	0.06
CHY014	120.5828	23.2963	66.3	37.16	0.26
CHY015	120.4052	23.3550	68.9	40.99	0.15
CHY016	120.1532	23.2212	96.8	70.06	0.11
CHY017	120.2680	23.2147	89.8	61.89	0.05
CHY019	120.4778	23.1795	82.2	53.04	0.07
CHY022	120.4615	23.0457	96.6	67.41	0.06
CHY023	120.2800	22.9655	112.4	83.36	0.06
CHY026	120.4113	23.7987	40.1	29.32	0.08
CHY027	120.2468	23.7520	57.6	45.81	0.05
CHY032	120.2944	23.5799	60.1	40.45	0.09
CHY033	120.2153	23.5407	69.3	49.04	0.07
CHY034	120.5443	23.5212	45.7	18.19	0.30
CHY036	120.4788	23.6073	43.1	21.46	0.27
CHY039	120.3440	23.5207	59.8	36.76	0.12
CHY042	120.5833	23.3583	59.8	30.67	0.10
CHY044	120.1635	23.3832	83.7	59.53	0.07
CHY047	120.4468	23.4938	54.2	28.22	0.18
CHY050	120.4083	23.2803	75.6	47.02	0.11
CHY052	120.5010	23.2878	70.3	41.22	0.15
CHY055	120.2705	23.2698	84.8	57.46	0.10
CHY057	120.4098	23.1495	88.2	59.10	0.05
CHY059	120.1025	23.1840	103.3	76.68	0.05
CHY060	120.2392	23.1243	99.6	71.30	0.05
CHY061	120.5107	23.0768	91.7	62.55	0.04
CHY062	120.4500	23.1213	89.3	60.08	0.06
CHY065	120.3450	22.9060	115.5	86.22	0.12
CHY066	120.2078	22.9205	120.4	91.44	0.05
CHY067	120.1837	22.9990	114.3	85.69	0.06
CHY069	120.1815	22.9737	116.8	88.08	0.04
CHY070	120.2286	22.9651	115.0	86.14	0.05
CHY071	120.1645	23.0648	109.4	81.26	0.08
CHY075	119.5552	23.5672	131.0	115.80	0.04
CHY079	120.5280	23.1848	79.8	50.63	0.05
CHY081	120.4965	23.2703	72.3	43.16	0.05
CHY082	120.2975	23.7237	53.4	40.48	0.08
CHY086	120.5932	23.3510	60.2	31.07	0.21
CHY088	120.4293	23.3462	68.3	40.02	0.21
CHY090	120.2163	23.2673	88.6	61.85	0.08
CHY092	120.4783	23.7913	33.6	22.46	0.11
CHY093	120.1472	23.6538	70.3	55.39	0.07
CHY096	120.2327	22.9830	113.1	84.25	0.04
CHY099	120.2802	23.1373	96.0	67.54	0.06
CHY100	120.3418	23.2272	84.3	55.84	0.07
CHY104	120.4648	23.6695	40.1	23.13	0.18
CHY107	120.2897	23.2988	81.1	53.86	0.10
CHY109	120.5295	23.2517	72.8	43.63	0.05
CHY110	120.5295	23.2517	72.8	43.63	0.03
CHY111	120.2273	23.7912	58.8	48.02	0.09
CHY112	120.1830	23.7035	65.2	52.03	0.10
CHY114	120.1187	23.0372	114.7	86.65	0.05
CHY115	120.0967	23.1543	106.1	79.23	0.06
CHY116	120.1082	23.0775	111.8	84.15	0.06
ENA	121.7407	24.4280	114.5	66.30	0.07
ESL	121.4328	23.8137	64.7	44.71	0.07
HEN	120.7380	22.0055	205.5	178.16	0.03
HSN	120.9695	24.8022	105.7	53.16	0.08
HWA	121.6050	23.9770	83.0	54.47	0.12
HWA003	121.4970	23.4768	82.9	53.53	0.14
HWA005	121.4140	23.6608	66.4	43.77	0.15
HWA006	121.4173	23.6732	66.3	44.00	0.09
HWA007	121.6173	23.9877	84.4	55.40	0.09
HWA009	121.6165	23.9925	84.5	55.21	0.10
HWA011	121.5858	23.9962	81.5	52.12	0.10
HWA012	121.6233	23.9930	85.1	55.86	0.08
HWA013	121.5910	23.9780	81.6	53.08	0.14
HWA014	121.5993	23.9732	82.4	54.02	0.10
HWA015	121.5530	23.9757	77.8	49.48	0.11
HWA016	121.5600	23.9648	78.3	50.49	0.10
HWA017	121.5392	23.9497	76.0	49.04	0.09
HWA022	121.7325	24.2675	105.1	64.59	0.12
HWA023	121.5955	24.0800	84.6	51.95	0.04
HWA025	121.6447	24.1630	92.3	56.39	0.07
HWA028	121.6013	24.0172	83.5	53.21	0.10
HWA029	121.5702	23.9373	78.9	52.40	0.09
HWA030	121.4488	23.7852	66.7	46.28	0.08
HWA031	121.4922	23.7653	71.4	50.39	0.10
HWA036	121.3670	23.4995	70.3	41.47	0.07
HWA039	121.3523	23.3845	77.2	45.48	0.08
HWA041	121.2942	23.2675	82.8	50.04	0.09
HWA044	121.5268	23.6538	77.6	54.20	0.08
HWA046	121.6213	24.1492	89.5	54.13	0.09
HWA048	121.5715	24.0113	80.4	50.39	0.17
HWA049	121.5577	23.9952	78.6	49.41	0.10
HWA050	121.5840	23.9897	81.1	52.10	0.09
HWA051	121.5480	23.8703	76.2	53.35	0.17
HWA053	121.3117	23.4072	72.5	41.22	0.03
HWA054	121.3398	23.4317	72.7	41.97	0.05
HWA055	121.3323	23.3232	80.6	48.08	0.09
HWA059	121.5005	23.8713	71.4	49.17	0.14
HWA060	121.5900	23.8703	80.5	57.09	0.04
HWA2	121.6050	23.9770	83.0	54.47	0.14
ILA001	121.8360	24.8827	154.5	97.33	0.03
ILA002	121.7973	24.8450	148.8	91.66	0.07
ILA003	121.7813	24.7982	143.9	87.18	0.07
ILA004	121.7828	24.7450	139.9	83.86	0.07
ILA005	121.8052	24.6978	138.0	82.99	0.08
ILA006	121.8250	24.6412	135.4	81.81	0.08
ILA007	121.8462	24.5943	133.8	81.67	0.09
ILA008	121.7628	24.7088	135.6	79.98	0.08
ILA012	121.7335	24.7807	139.2	82.20	0.08
ILA013	121.7294	24.7350	135.3	78.82	0.15
ILA014	121.7202	24.6945	131.4	75.52	0.06
ILA015	121.6912	24.7807	136.3	78.92	0.05
ILA016	121.6840	24.7490	133.2	76.12	0.08
ILA021	121.6440	24.7135	127.6	70.54	0.07
ILA027	121.7603	24.6893	134.0	78.62	0.10
ILA030	121.7550	24.7278	136.5	80.48	0.12
ILA031	121.8337	24.5995	133.2	80.72	0.08
ILA032	121.8272	24.6242	134.4	81.21	0.06
ILA035	121.7603	24.8241	144.6	87.32	0.07
ILA036	121.7513	24.7883	141.1	84.12	0.07
ILA037	121.7142	24.7455	135.0	78.28	0.11
ILA039	121.7212	24.7650	137.1	80.15	0.06
ILA041	121.7917	24.7233	138.9	83.30	0.10
ILA042	121.7920	24.6903	136.4	81.42	0.08
ILA043	121.7347	24.6290	127.6	73.10	0.06
ILA044	121.7550	24.6560	131.1	76.30	0.08
ILA046	121.7338	24.6660	130.2	75.01	0.07
ILA048	121.7612	24.7663	140.0	83.44	0.09
ILA049	121.7480	24.7655	139.0	82.32	0.08
ILA050	121.7407	24.4280	114.5	66.30	0.06
ILA052	121.8488	24.6092	135.0	82.54	0.04
ILA054	121.9183	24.9732	167.5	110.16	0.03
ILA055	121.8083	24.7387	141.3	85.62	0.08
ILA056	121.8088	24.7622	143.1	87.10	0.07
ILA059	121.8205	24.6667	136.8	82.67	0.07
ILA064	121.7787	24.4770	120.7	71.44	0.07
ILA066	121.7707	24.4473	118.2	69.66	0.10
KAU001	120.6355	23.1618	79.2	50.74	0.04
KAU003	120.2573	22.6280	147.3	118.06	0.02
KAU006	120.3173	22.5910	149.0	119.80	0.02
KAU007	120.3585	22.6462	141.8	112.69	0.03
KAU008	120.3672	22.6295	143.3	114.20	0.03
KAU010	120.2790	22.7873	130.2	100.97	0.03
KAU011	120.2558	22.7613	133.8	104.58	0.06
KAU012	120.3707	22.8797	117.1	87.89	0.09
KAU015	120.3317	22.6560	141.7	112.51	0.03
KAU017	120.3862	22.5090	155.5	126.55	0.03

Table 2. (continued)

Station	Log	Lat	Epi	D_{rup}	PGA
KAU018	120.4738	22.8910	112.4	83.36	0.04
KAU022	120.4910	22.6707	135.5	106.75	0.03
KAU030	120.5588	22.6108	140.6	112.24	0.04
KAU032	120.4528	22.5462	149.8	121.03	0.04
KAU033	120.4535	22.4643	158.6	129.92	0.03
KAU034	120.6195	22.5290	148.6	120.73	0.01
KAU037	120.6432	22.2617	177.8	150.17	0.03
KAU038	120.6853	22.1922	185.1	157.69	0.01
KAU039	120.7418	22.0982	195.2	167.89	0.01
KAU040	120.8703	22.1905	185.1	157.43	0.01
KAU042	120.8292	22.0225	203.5	176.05	0.01
KAU043	120.8403	21.9137	215.6	188.05	0.02
KAU044	120.5028	22.4397	160.2	131.78	0.04
KAU045	120.3080	22.5678	151.7	122.54	0.03
KAU046	120.7380	22.0055	205.5	178.16	0.02
KAU047	120.5827	23.0817	89.0	60.29	0.04
KAU048	120.4908	22.7252	129.6	100.83	0.04
KAU052	120.8053	21.9433	212.3	184.85	0.01
KAU055	120.3353	22.5747	150.1	120.96	0.03
KAU056	120.3437	22.5538	152.0	122.92	0.02
KAU057	120.2633	22.6342	146.5	117.20	0.02
KAU058	120.3203	22.6495	142.8	113.57	0.02
KAU062	120.2843	22.6237	146.7	117.51	0.03
KAU063	120.1732	22.9053	123.6	94.78	0.04
KAU064	120.2385	22.7852	132.2	102.96	0.04
KAU066	120.3412	22.7303	133.6	104.43	0.04
KAU073	120.5362	22.5348	149.2	120.88	0.03
KAU074	120.5663	22.5740	144.4	116.21	0.03
KAU075	120.4990	22.4903	154.8	126.30	0.04
KAU077	120.7233	22.7470	123.5	96.23	0.02
KAU078	120.6412	22.7112	128.3	100.46	0.05
KAU081	120.7367	22.0095	205.1	177.72	0.03
KAU082	120.7238	21.9428	212.5	185.14	0.02
KAU083	120.4475	22.5673	147.7	118.85	0.03
KAU085	120.3222	22.8858	118.4	89.22	0.05
KAU086	120.2950	22.7950	128.8	99.52	0.05
KAU087	120.3113	22.6128	146.9	117.71	0.03
KAU088	120.3110	22.6461	143.5	114.24	0.03
KAU089	120.4028	22.4802	158.1	129.26	0.03
LAY	121.5507	22.0387	215.9	182.11	0.01
NCU	121.1867	24.9700	129.0	73.03	0.10
NSK	121.3583	24.6755	106.6	48.02	0.07
NST	121.0005	24.6312	87.8	34.85	0.40
NSY	120.7607	24.4162	61.7	9.08	0.12
PNG	119.5552	23.5672	131.0	115.80	0.03
SGL	120.4908	22.7252	129.6	100.83	0.04
SGS	120.5827	23.0817	89.0	60.29	0.04
SSD	120.6320	22.7460	124.6	96.66	0.03
STY	120.7573	23.1625	77.4	50.29	0.04
TAI1	120.2283	23.0402	108.0	79.31	0.09
TAP	121.5225	25.0392	149.8	90.65	0.06
TAP003	121.4500	25.0863	151.0	92.23	0.13
TAP005	121.5070	25.1077	155.7	96.71	0.13
TAP006	121.5093	25.0947	154.5	95.51	0.10
TAP007	121.5083	25.0758	152.6	93.59	0.11
TAP008	121.5273	25.0758	153.5	94.45	0.08
TAP010	121.4813	25.0677	150.5	91.62	0.12
TAP012	121.5078	25.0563	150.7	91.65	0.10
TAP013	121.5253	25.0572	151.6	92.54	0.09
TAP014	121.5442	25.0578	152.6	93.50	0.11
TAP017	121.4480	25.0528	147.5	88.75	0.11
TAP020	121.5263	25.0388	149.9	90.80	0.07
TAP021	121.5432	25.0378	150.7	91.52	0.10
TAP024	121.4652	25.0203	145.1	86.20	0.08
TAP026	121.5027	25.0170	146.6	87.56	0.08
TAP028	121.5073	25.0045	145.6	86.56	0.05
TAP032	121.4748	25.0007	143.7	84.68	0.12
TAP034	121.5303	24.9550	142.1	83.00	0.06
TAP035	121.5399	24.9239	139.7	80.64	0.09
TAP036	121.5447	24.9043	138.2	79.12	0.04
TAP041	121.4167	25.1830	159.3	101.06	0.09
TAP042	121.4532	25.1255	155.0	96.35	0.10
TAP043	121.4100	24.9913	139.7	81.02	0.08

Table 2. (continued)

Station	Log	Lat	Epi	D_{rup}	PGA
TAP046	121.7683	25.1037	169.2	110.22	0.08
TAP047	121.3375	24.9538	132.8	74.59	0.05
TAP049	121.4365	25.1480	156.6	98.08	0.12
TAP051	121.4403	25.1008	152.0	93.34	0.11
TAP052	121.3828	25.0817	147.6	89.39	0.13
TAP053	121.5143	24.9590	141.7	82.61	0.08
TAP059	121.6855	25.1565	169.3	110.16	0.04
TAP060	121.7237	25.1572	171.5	112.34	0.04
TAP065	121.7668	25.1488	173.1	114.10	0.04
TAP066	121.5202	25.1865	164.1	105.25	0.07
TAP067	121.5802	24.9802	147.2	88.07	0.04
TAP069	121.9882	25.0082	175.2	118.05	0.04
TAP072	121.6500	24.9913	152.1	93.11	0.05
TAP075	121.7280	25.0288	160.0	101.22	0.08
TAP077	121.8437	25.0643	170.3	111.81	0.03
TAP078	121.8595	25.0354	168.8	110.58	0.04
TAP079	121.9060	25.0237	170.9	113.00	0.03
TAP081	121.9808	25.0182	175.5	118.19	0.03
TAP083	121.4938	25.2595	170.2	111.63	0.06
TAP084	121.6295	25.2252	173.0	113.85	0.04
TAP086	121.5677	24.9527	143.9	84.84	0.05
TAP087	121.4177	25.1008	151.0	92.54	0.08
TAP088	121.5762	25.0385	152.4	93.26	0.12
TAP089	121.5595	25.0270	150.5	91.31	0.04
TAP090	121.5945	25.0573	155.2	95.99	0.14
TAP094	121.4758	25.1410	157.5	98.80	0.09
TAP095	121.4913	25.1353	157.7	98.83	0.14
TAP097	121.5299	25.0207	148.3	89.22	0.08
TAP098	121.5395	25.1030	156.8	97.81	0.06
TAP100	121.5139	25.0351	148.9	89.85	0.09
TAP103	121.7810	25.0710	167.0	108.27	0.17
TAP104	121.7202	25.1580	171.4	112.22	0.04
TAW	120.8957	22.3575	166.7	138.98	0.00
TCU	120.6760	24.1475	34.2	4.47	0.20
TCU003	121.1357	25.0473	135.8	81.09	0.08
TCU006	121.1405	24.9118	121.5	66.28	0.08
TCU007	121.3097	25.0015	136.6	78.79	0.07
TCU008	121.2062	25.0092	133.8	77.54	0.07
TCU009	121.2200	24.9655	129.6	73.00	0.07
TCU010	121.1533	25.0003	131.3	76.05	0.09
TCU011	121.2783	24.8855	123.5	65.67	0.07
TCU014	121.3075	25.0463	141.1	83.50	0.08
TCU015	120.9345	24.7572	100.3	48.01	0.13
TCU017	121.0068	24.7808	104.1	51.08	0.13
TCU018	121.0535	24.8800	115.8	62.22	0.06
TCU025	121.1760	24.7065	101.2	44.45	0.08
TCU031	120.7010	24.5615	78.3	24.88	0.12
TCU034	120.8568	24.6390	86.4	34.48	0.25
TCU035	120.7877	24.6157	83.7	31.10	0.12
TCU036	120.6963	24.4488	66.0	12.71	0.14
TCU040	120.6455	24.4497	67.1	15.02	0.16
TCU042	120.8077	24.5542	76.9	24.63	0.25
TCU047	120.9387	24.6188	85.2	33.03	0.41
TCU048	120.5888	24.1800	41.4	13.43	0.18
TCU050	120.6338	24.1815	39.4	8.89	0.15
TCU051	120.6518	24.1603	36.5	6.95	0.23
TCU055	120.6643	24.1392	33.8	5.58	0.26
TCU056	120.6238	24.1588	37.6	9.76	0.16
TCU057	120.6107	24.1732	39.6	11.17	0.11
TCU061	120.5490	24.1355	39.7	17.20	0.16
TCU081	120.9695	24.8022	105.7	53.16	0.09
TCU082	120.6760	24.1475	34.2	4.47	0.23
TCU083	121.1867	24.9700	129.0	73.03	0.12
TCU092	121.2792	25.0117	136.5	79.13	0.09
TCU094	121.0488	24.7695	103.8	50.13	0.09
TCU096	120.9558	24.7957	104.8	52.35	0.11
TCU098	120.8990	24.7433	98.3	46.25	0.11
TCU100	120.6153	24.1858	40.6	10.78	0.11
TCU101	120.7092	24.2420	43.3	1.90	0.26
TCU104	120.6018	24.2455	47.2	12.50	0.10
TCU105	120.5590	24.2390	48.6	16.78	0.13
TCU106	120.5518	24.0833	35.3	16.66	0.16
TCU107	120.5402	24.0727	35.4	17.78	0.15

Table 2. (continued)

Station	Log	Lat	Epi	D_{rup}	PGA
TCU110	120.5695	23.9622	26.0	14.16	0.19
TCU111	120.4872	24.1137	42.4	23.37	0.13
TCU113	120.3865	23.8928	42.2	32.39	0.08
TCU115	120.4693	23.9595	35.4	24.35	0.12
TCU118	120.4235	24.0027	41.4	29.26	0.12
TCU119	120.3122	23.9242	50.1	40.14	0.06
TCU131	120.8165	24.5673	78.3	26.15	0.12
TCU138	120.5955	23.9223	21.9	11.29	0.21
TCU145	120.3368	23.9800	48.9	37.96	0.07
TTN	121.1465	22.7540	127.6	96.67	0.03
TTN001	121.4425	23.3178	89.0	56.23	0.10
TTN002	121.2968	22.9738	110.6	77.27	0.03
TTN003	120.9975	22.6178	139.1	110.51	0.02
TTN004	121.1287	22.9102	110.5	79.78	0.04
TTN005	121.1403	22.7568	127.1	96.29	0.03
TTN006	121.1378	22.7717	125.4	94.67	0.03
TTN007	121.1427	22.7647	126.3	95.48	0.03
TTN008	121.1517	22.7602	127.0	96.07	0.03
TTN009	121.1442	22.7488	128.0	97.20	0.03
TTN010	121.1135	22.7400	128.2	97.83	0.03
TTN012	121.1330	22.7662	125.9	95.20	0.03
TTN013	121.1277	22.7678	125.6	94.97	0.02
TTN014	121.3653	23.0992	102.2	68.29	0.05
TTN015	121.1465	22.7540	127.6	96.67	0.03
TTN016	120.8957	22.3575	166.7	138.98	0.01
TTN018	121.0717	22.8207	118.5	88.85	0.04
TTN020	121.2057	23.1268	91.2	59.14	0.04
TTN022	121.2105	23.0973	94.4	62.20	0.08
TTN023	121.1557	23.0530	96.5	65.28	0.07
TTN024	121.1083	22.9725	103.3	72.96	0.03
TTN026	121.0830	22.8630	114.2	84.40	0.04
TTN027	121.0860	22.8078	120.2	90.32	0.04
TTN028	121.0543	22.7790	122.6	93.23	0.02
TTN032	121.4055	23.2462	91.9	58.46	0.08
TTN036	121.1855	22.7988	124.0	92.47	0.03
TTN040	121.1980	23.1512	88.5	56.52	0.03
TTN045	121.1478	22.9757	104.2	73.17	0.04
TTN046	121.2320	22.9658	108.5	76.06	0.11
TTN047	121.1310	22.8402	118.0	87.27	0.03
TTN048	121.0827	22.7730	123.9	94.04	0.03
TTN049	121.1003	22.7320	128.7	98.59	0.26
TTN050	121.0293	22.6740	133.5	104.49	0.03
WGK	120.5622	23.6862	30.9	13.31	0.46
WNT	120.6843	23.8783	11.9	2.21	0.94
WSF	120.2217	23.6380	63.8	47.71	0.07
WTC	120.2812	23.8635	52.8	42.95	0.05
WTP	120.6138	23.2455	70.7	41.89	0.05

The columns are the same as defined in Table 1.

Taiwan, the set B stations are far from the set A stations. Simulation results show that in west and east Taiwan, the ground motions at the localities near the earthquake source are mainly influenced by the source-slip distribution. Meanwhile, the simulated waveforms at both set A and set B stations in the two areas have better fit with the observed seismograms because of the well-established source slip model. In north and south Taiwan, since the set B stations mostly have larger distances to the surface break, the path effect is higher for the set B stations than for the set A ones. Because of the northward rupture propagation during the earthquake, the ground motions are characterized by long periods (around 10 s) and large amplitudes in north Taiwan. This strong directivity effect can be clearly seen in synthetic waveforms at both set A and set B stations in this region. In the opposite, the directivity effect is weak in south Taiwan; the site effect remarkably influences the ground motions. However, the site effect cannot be simulated on the basis of the given velocity model. Thus only at some set B stations in south Taiwan the simulated waveforms can fit well with the observed seismograms. It is notable that the synthetic waveforms at some set B stations in the Taipei Basin can be comparable with the observed seismograms, yet with different amplitudes such as TAP032 (Figure 2b). This might be due to a strong site effect caused by the basin properties, including basin geometry, low-velocity materials, and topography (S. J. Lee, et al., Mesh generation and strong ground motion simulations in the Taipei basin based upon the spectral-element method, submitted to *Bulletin of the Seismological Society of America*, 2007). Furthermore, if the higher-accuracy three-dimensional velocity model can be used for the calculation of Green's functions and also for the forward simulation, the discrepancy will certainly be reduced.

[16] Although the recorded island-wide ground motions show waveforms of high complexity, the forward synthetic results can basically reproduce most of the waveform features over the frequency band below 0.5 Hz. This good agreement indicates that the Chi-Chi rupture source model derived from earlier inversion, the three-dimensional crustal structure from traveltime tomography, as well as the numerical codes used are satisfactory, or at least they are internally consistent. We venture to state that for sites without strong motion records, this simulation can basically predict the strong ground shaking excited by the Chi-Chi main shock. This capability would allow large-scale assessment of building performance in Taiwan, such as the famous Taipei 101 building experiencing a Chi-Chi-like excitation.

3.2. Strong Ground Motion Snapshot

[17] We use all data stored in our numerical simulation to construct a series of snapshots showing how the wavefield is generated from the Chelungpu rupture source and propagating outward, crossing the mountain range, and interacting with the sedimentary terrain. Figure 3 shows the vertical velocity wavefield at 100 s after the initiation of the rupture. The source-slip distribution at the same moment is also shown at the lower right part. At the beginning, the ground shaking is not obvious because the initial slip is weak and located in a deeper part of the crust around the nucleation area. Fifteen seconds later, the rupture front encountered the first major asperity at the middle section of the Chelungpu fault near the TsaoTun area which resulted in a strong excitation. The rupture front almost stops at TsaoTun and at the same time continued releasing energy for about 10 s before moving on. Toward the last stage of the rupture, the largest slip occurred around the northern bend at about 22$\sim$27 s after the initiation. New shaking, excited by this slip event joining the energy coming from the northward-propagating front generated by the rupture of the fist asperity 10 s earlier, resulted in the largest ground motions (more than 1500 cm displacement and nearly 300 cm/s in velocity) near Shihkang-FongYuan area. This strong shaking had a very long duration and continued the same motion in a broad area for about 10 s. Subsequently, the zone experiencing long-period shaking expanded and began to radiate energy outward, with an apparent directivity toward northern Taiwan at about the 37th second. This anomalous shaking phenomenon reminds

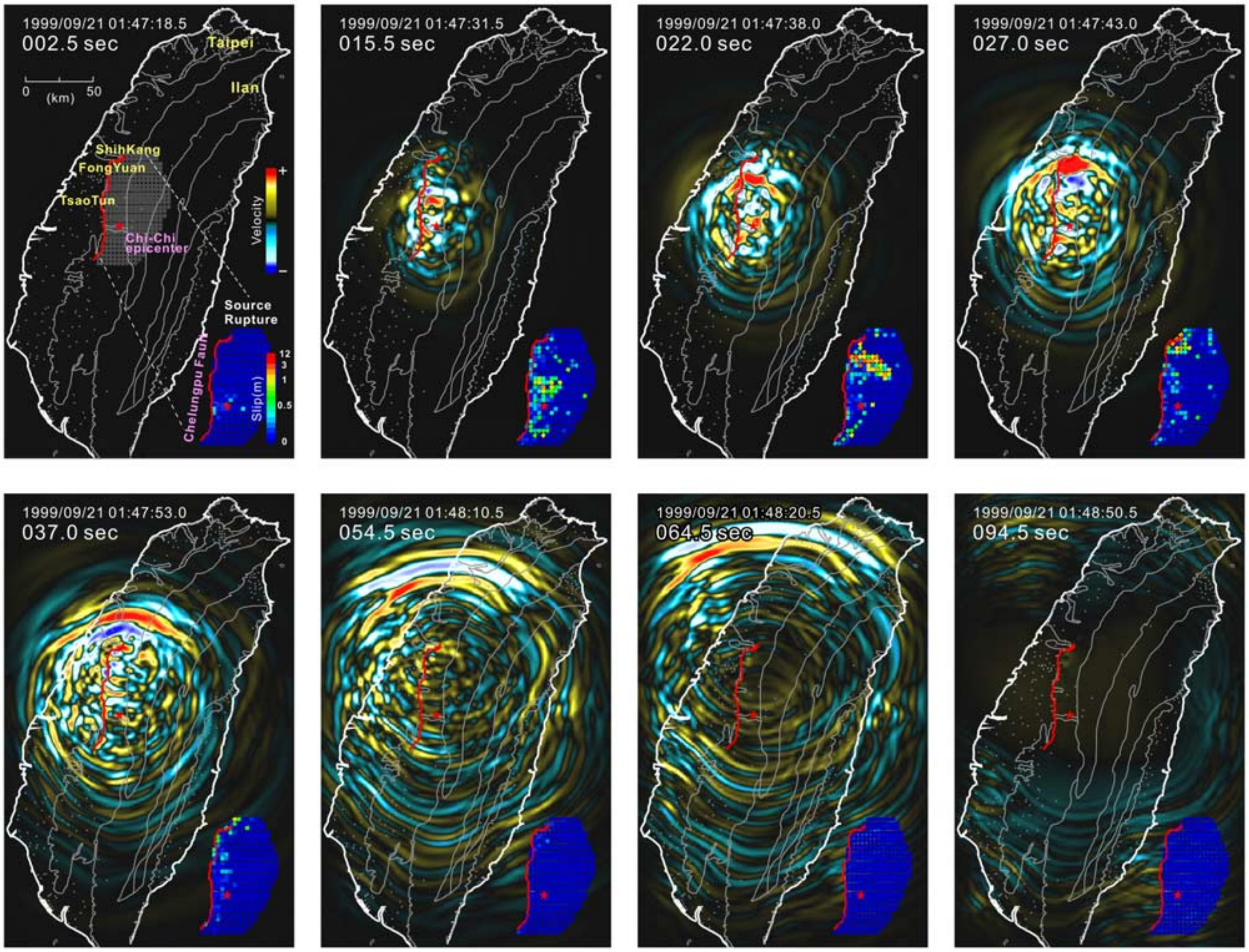

Figure 3. Vertical velocity wave-field snapshot 100 s after the initial rupture. Eight meaningful snapshots are shown. They are 2.5th, 15.5th, 22.0th, 27.0th, 37.0th, 54.5th, 64.5th, and 94.5th s, respectively. The absolute local time is also presented at the top of each snapshot. Lower right panel shows the source slip distribution at the same moment to the wave-field snapshot. The amplitudes of ground velocity value and source slip amount are described as the color labels in the first snapshot.

one of a similar behavior of a tornado; in its progression, it dwells at a location, continuing to emit destructive energy before moving on. When the wavefield moves on, a northward directivity is again apparent. Yet the south-propagating ground motion toward the southern part of the fault is relatively small, again, because of the nature of the northward-propagating Chelungpu rupture. At the 50th$\sim$55th second, the large-amplitude ground motion entered northwest Taiwan. The Taipei metropolitan area, situated in the shallow basin of low-velocity sediments, experienced substantial site amplification from this long-period propagating front of strong shaking at about 1 min after the rupture initiation. As waves entered the Taipei basin and the Ilan plain, it reverberated for another 30 s, while shaking in most other parts of Taiwan had long subsided. Although the resolution of the three-dimensional velocity structure derived from traveltime tomography cannot really resolve the thin (<1 km) basin sediments, nonetheless the site amplification still can be revealed. Our simulation confirms the fact that the extended damage in the Taipei basin and Ilan plain, some 140 km away, is a combined result of a large rupture, rupture directivity, and local site amplification. This confirmation is not possible without the extensive TSMIP strong motion data recovery.

3.3. PGV Simulation

[18] The synthetic PGV distribution is derived by band-passing all three component velocity wavefields from 0.01 to 0.5 Hz and then plotting the peak values of the ground velocity on a map. This map is compared to an observed PGV map with the same frequency band. A comparison between observed and synthetic data is given in Figure 4. Both the observed and simulated PGV distributions indicate that the hanging wall of the Chelungpu fault has much larger PGV values on all three components. Maximum values are located at the northern bend of the fault. However, as shown in the synthetic PGV (Figure 4b), the contours of largest PGV values are distributed more narrowly as compared to that observed (Figure 4a). This discrepancy may come from the lack of station coverage especially at the eastern side close to the mountainous area. By taking advantage of a fine grid interval (0.5 km),

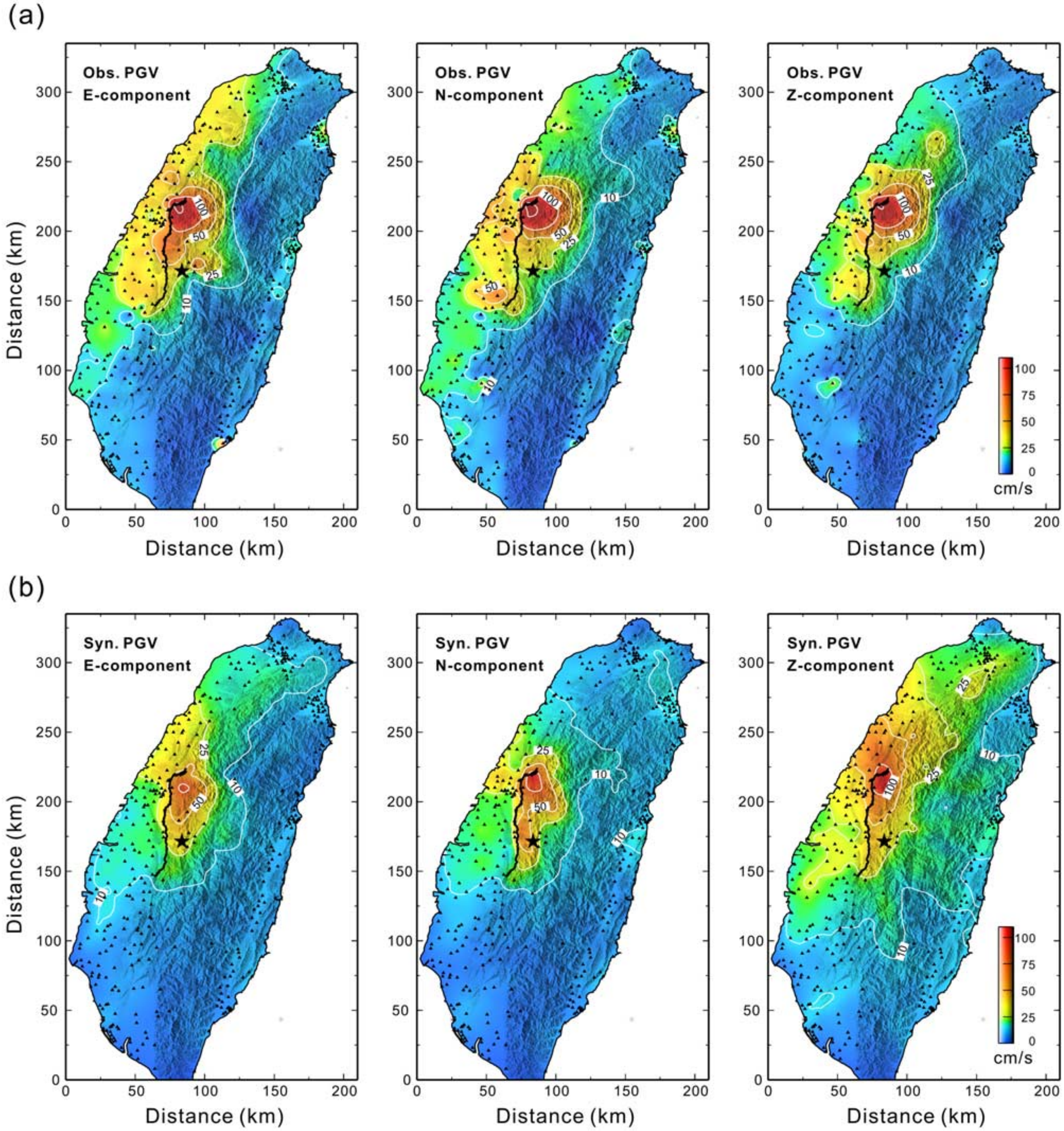

Figure 4. Comparison of the PGV distribution between observed and simulated results. (a) The observed *E*, *N*, and *Z* component PGV distribution. (b) The simulated three-component PGV distribution. All the results are band-pass filtered by a corner frequency of 0.01–0.5 Hz and using the same PGV color scale at the lower right. The results indicate that the hanging wall has large PGV value in all three components, especially at the northern end of the Chelungpu fault. A directivity effect is also present in both synthetics and observations of all components.

forward simulation results probably can reproduce a more complete coverage of PGV without artificial interpolation. A strong directivity effect can be identified in both observed and synthetic PGV which show the 10 cm/s peak ground velocity area extending from source rupture region to most of the northern Taiwan. Furthermore, the PGV values in the Central Range (where there is little TSMIP coverage) and southern Taiwan are weak. Beyond the Central Range along the Longitudinal Valley and Ilan plain, anomalous PGV values observed are due to soft-sediments amplifications. Although the three-dimensional velocity model used in our study does not have high enough resolution to explain the near-surface effect, these amplification phenomena can still be seen numerically. The results also suggest that these local

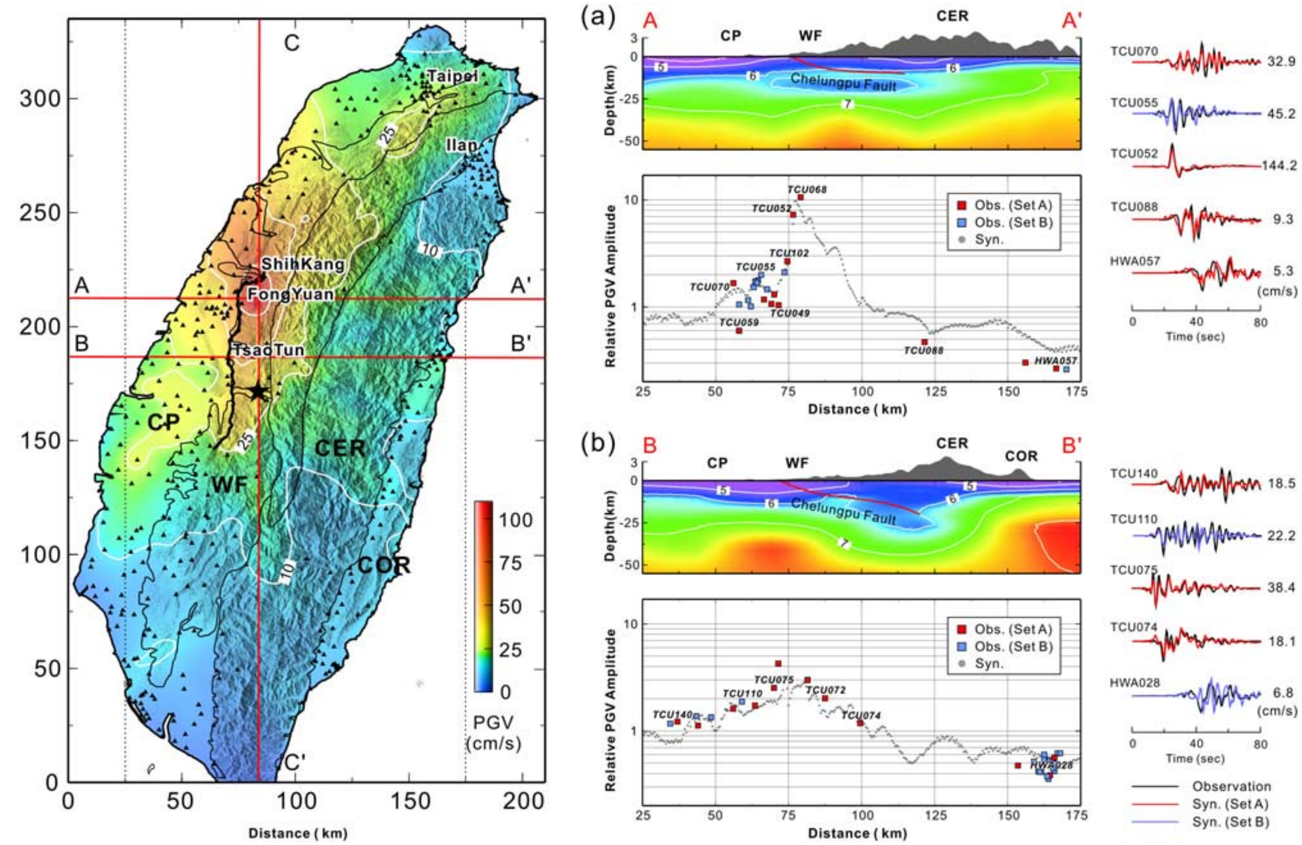

Figure 5. The relation between velocity structure, fault slip, and peak ground velocity. Left panel is the vertical-component surface PGV distribution. Two profiles are used in the comparison: A-A′ profile ranges across the largest asperity at the northern bending tip of Chelungpu fault; the B-B′ profile ranges across the secondary asperity at the middle part of the fault. C-C′ profile is a north-south cross section used in the snapshot analysis as described in Figure 8. In the left panel, (a) the velocity profile and PGV values of both synthetic (gray circle) and observation (red square indicates set A station and blue square indicates set B) across the A-A′ profile; and (b) the results on the B-B′ profile. Also shown in the left panels are the waveforms of the stations close to the profile for comparison.

larger PGV values may also have a contribution from the deep structure.

[19] In order to examine the relation among the three-dimensional velocity structure, the fault slip, and the resulting PGV distributions, we analyze two west-east profiles across the two principal asperities as shown in Figure 5. The A-A′ profile is across the north largest asperity near Shihkang-FongYuan area (Figure 5a). Although the slip on the fault is highly variable, the comparison between observed and simulated PGV shows good agreement. The largest PGV values occur near the surface break of the fault, as recorded by TCU068 and TCU052. The synthetic PGV values explain these peaks quite well. Stations at the footwall have a more complex PGV distribution even within a short distance. Simulated PGV values can almost follow their average trend. In the eastern part of the profile, the forward-simulated result somewhat overestimates the observations with a discrepancy of about twofold, such as at HWA057. Figure 5b shows the result on profile B-B′. In this profile, most of the synthetic PGV values can basically explain the PGV trend of observations well. Again, the stations in the eastern part show larger variations and have larger discrepancies with the synthetics. This may be due to the influence of local site effect which cannot adequately be reflected by the used tomography model. Although part of the forward simulation results have some discrepancies in peak ground-velocity values compared to observations, the related waveforms, as shown on the left side of both Figures 5a and 5b, can basically fit observations in both traveltime and waveform.

[20] With a three-dimensional spatiotemporal source model (from inversion) and an adequate three-dimensional crustal velocity, we show an enhancement in the accuracy of PGV simulation. A high-resolution source model directly reflects the location of anomalously large PGV regions in areas close to the ruptured asperities. The directivity effect from the source rupture and three-dimensional lateral propagation effect due to crustal velocity anomalies are reflected by the PGV simulation clearly. Although the recent three-dimensional velocity model under Taiwan does not have a high enough resolution to reveal the low velocity of unconsolidated sediments and near-surface effect of some local site responses, synthetic velocity waveforms can

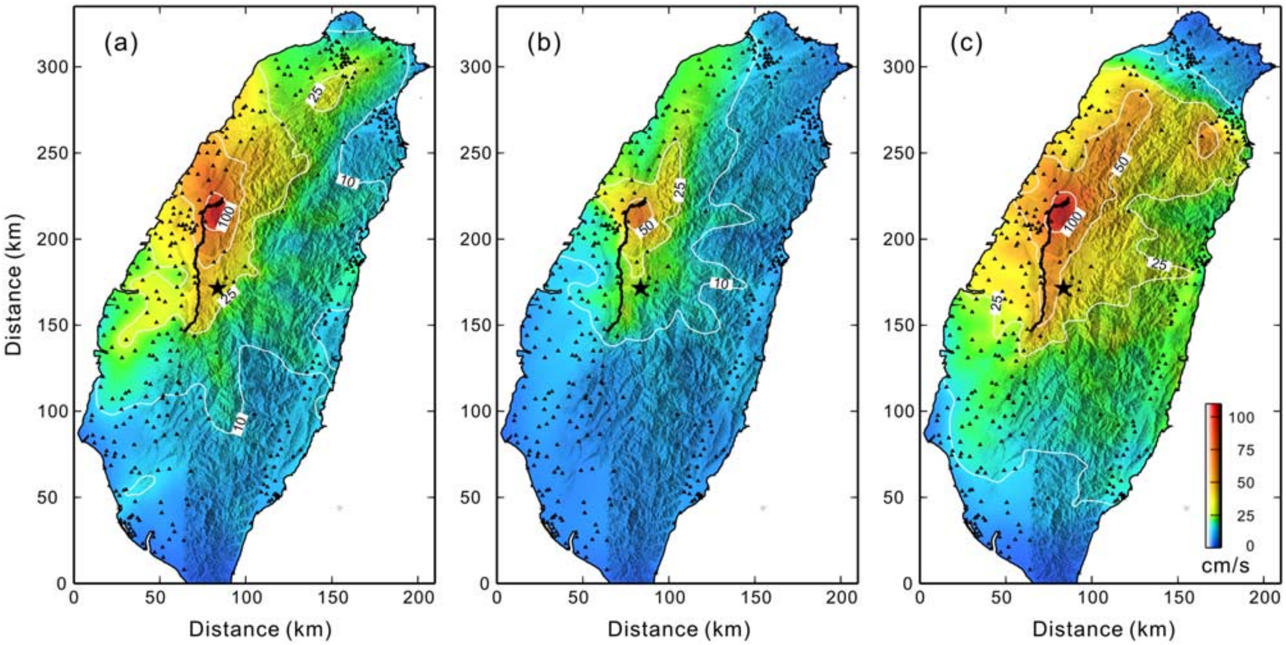

Figure 6. The influence of the velocity model on PGV distribution. We use an identical source rupture model derived from *Lee et al.* [2006b] to examine three different kinds of velocity structures. The three velocity models from left to right are the following: (a) the three-dimensional velocity model from *Rau and Wu* [1995], which is used in both the inversion and forward study; (b) a homogeneous half-space model, giving a V_p = 6.0 km/s and V_s = 3.464 km/s; and (c) a one-dimensional layered model [*Ho and Shin*, 1994]. The amplitude of PGV is presented by rainbow-like color scale.

basically explain most characteristics of the PGV distribution in low-frequency records.

4. Discussion

4.1. Influence of the Crustal Velocity Model

[21] To analyze the influence of the PGV distribution derived from the variations of velocity models, we compare simulation results from three different velocity models. One of the models from *Rau and Wu* [1995] is used in this study. The other two are a homogeneous half-space model (V_p = 6.0 km/s) and a one-dimensional layered model [*Ho and Shin*, 1994]. Figure 6 shows the simulated PGV distributions of these three models. Figure 6a gives the present results. Figure 6b gives the PGV distribution derive from one-dimensional homogeneous half-space model. This result can also be considered as the response of purely source effect. Overall PGV values in Figure 6b are low because large amount of energy is radiated into the earth interior, and the surface motions are excited primarily by direct arrivals; some directivity effect, however, is still seen. Figure 6c gives the result from a one-dimensional layered crustal model [*Ho and Shin*, 1994]; it deemphasizes azimuthal distribution and has a wider rainbow-like band of PGV distribution. The PGV value near the source region is comparable between layered model and three-dimensional tomography model [*Rau and Wu*, 1995]. While in the northern Taiwan, this one-dimensional layered crustal model gives an overestimated directivity effect. It also has a higher PGV value in southern Taiwan.

[22] From these results, we conclude that when the waveform of Green's function is weak or simple, as in the case of a homogenous half-space model, a larger slip amount on the fault will result after the source inversion because of energy loss into the half-space; it needs a stronger source effect to explain the observations. Notably, if Green's function is calculated from a one-dimensional layer model, it would cause an inversion result with a smaller seismic moment and a weaker slip on the fault because of the layered model which uniformly keeps radiated energy near the surface, thus producing overestimated reflections and later phases. Thus the source effect will be depressed to fit with the observations. This analysis indicates that using an adequate velocity model is crucial in both source inversion and strong motion forward simulation. The dominant influences from three-dimensional variations of earth structure cannot be underestimated especially in a geologically complex region like Taiwan.

4.2. Propagating Wave-Field Analysis

[23] In order to study the detailed relations between the three-dimensional lateral path effect, source energy radiation, and surface strong ground motion, we show the wavefield snapshots of two vertical profiles. The first profile follows a west-east direction across the asperity at middle section of the Chelungpu fault as shown in Figure 5 B-B′ profile. From west to east, this profile is across several tectonic settings including the West Costal Plain (CP), Western Foothill (WF), Central Range (CER), Longitude Valley (LV), and Costal Range (COR) (Figure 7a). In 16-s snapshot (Figure 7a), the asperity near the TasoTun area begins to release long-period, large-amplitude energy and continues for about 10 s. We can see the related strong shaking at the shallow part of the fault in this profile. At the

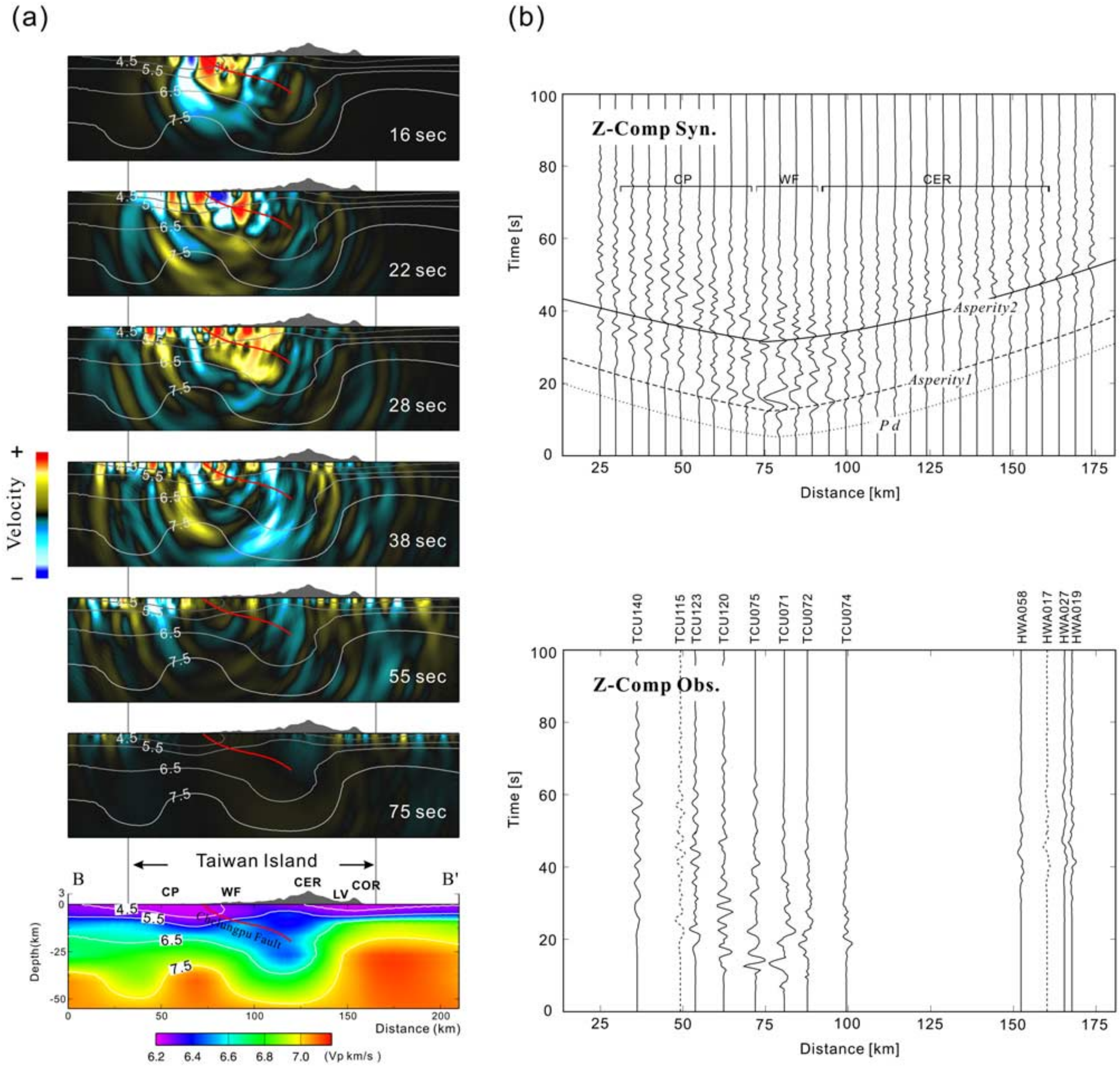

Figure 7. The propagating wave-field analysis of a west-east profile which crosses the middle part of the Chelungpu fault as shown in Figure 5 B-B′. (a) The velocity wave-field snapshots and velocity model across the profile. Red solid line indicates the cross section of Chelungpu fault. The surface topography (in a different scale) and main geological settings across the profile, including the Costal Plain (CP), Western Foothill (WF), Central Range (CER), and Costal Range (COR) are pointed out in the figure. (b) The comparison between observation and synthetic in vertical component velocity waveforms. The upper part is the synthetic waveforms shown by an interval of every 5 km. The traveltime curves, including direct wave and two main asperities, are represented by dotted and solid lines, respectively. Lower part is the record of the stations located within 10 km of the profile. Solid lines are the records at set A stations, dotted lines are set B stations.

38th second, the ground surface continues shaking for long duration because of the backward-propagating energy coming from largest north asperity. In general, most of the released energy is concentrated at the hanging wall of the Chelungpu fault. However, low-velocity material at the shallow part of west costal plain also produces apparent amplification in the footwall region. The synthetic waveforms along the profile are shown in the right panels (Figure 7b). Also shown in Figure 7b are the observed records close to the profile (within 10 km width) for comparison. From the synthetic waveform, it shows that the energy propagated into the Central Range (CER) is relative weak and decays quickly. Nevertheless, across the Longitude Valley (LV), the waveform is then amplified again. We can see from snapshots that the wavefields along the dipping direction of the Chelungpu fault have

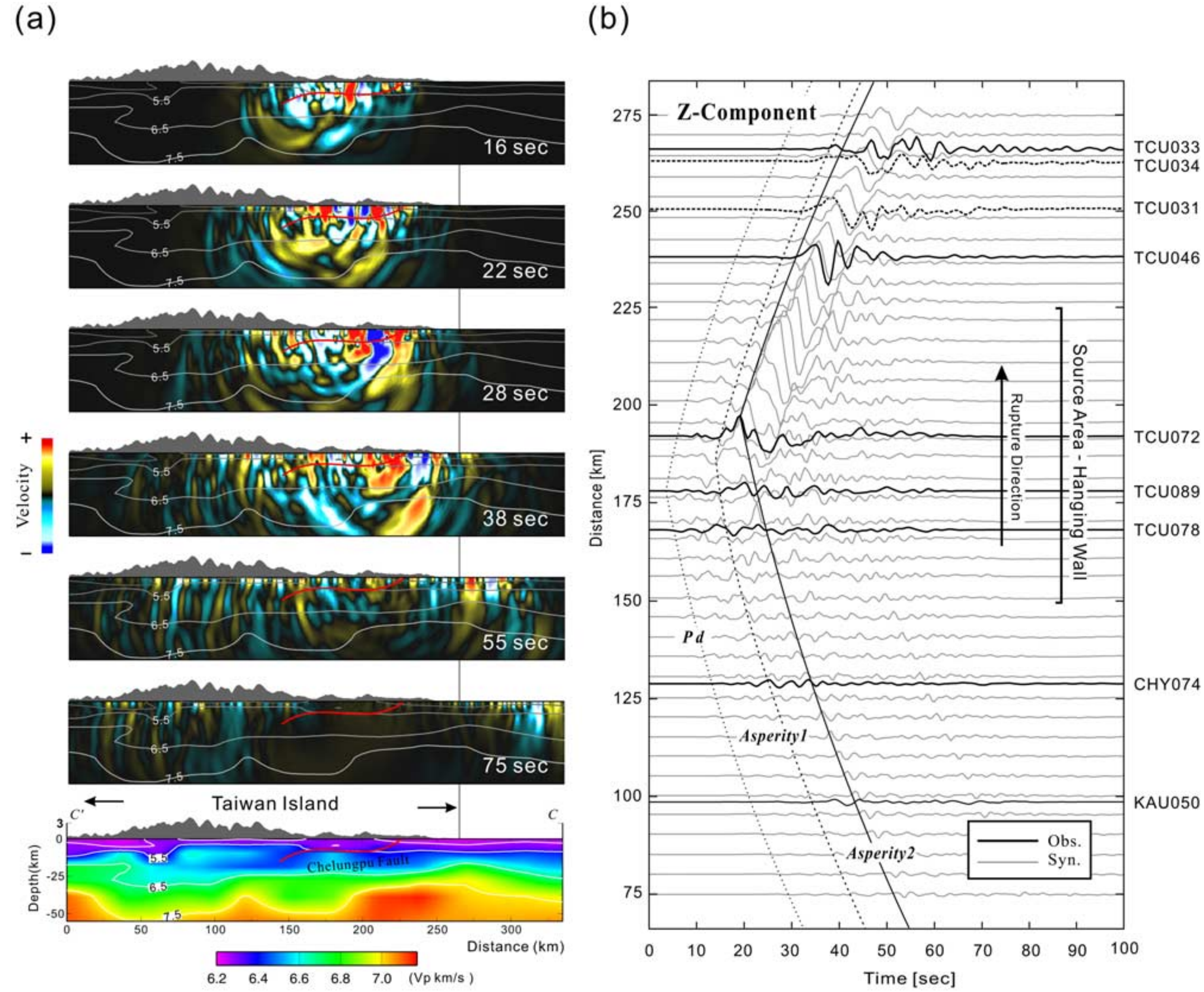

Figure 8. The propagating wave-field analysis of the north-south profile which cuts through the hanging wall of the Chelungpu fault (Figure 5 C-C′ profile). (a) The velocity wave-field snapshots and velocity model across the profile. Red solid line is the cross section of the Chelungpu fault. (b) Comparison between observation and synthetic waveforms in vertical component. Thick lines are the observation records from the stations located within 10 km of the profile. The records of set A stations are shown by solid lines, and set B stations are shown by dotted lines. Thin lines are synthetic waveforms along the profile with an interval of 5 km. The traveltime curve of the direct wave and two main asperities are represented by dotted lines and a solid line, respectively. The hanging wall source area and rupture direction are also represented in the figure.

been amplified. This is due to the characteristics of a thrust-faulting system. The radiation of energy in this case has an azimuthal maximum along a downdip direction. Thus most of the energy is released downward and results in a relatively weak ground motion at the ground surface in the Central Range. Unfortunately, this phenomenon is not easy to examine by observation because of the absence of records in mountainous areas.

[24] The second profile cuts through the hanging wall in a north-south direction. During the Chi-Chi earthquake, the rupture was mainly propagated from south to north along the Chelungpu fault. Because of this strong rupture property, the ground motion shows an obvious source rupture effect which is observed in the snapshots of this profile (Figure 8a). At the northern part of the fault, the strongest asperity released a large amount of rupture energy during the time frame of 22–28 s and combined with the energy radiating from an earlier asperity at TasoTun (in 16-s snapshot) to form an extremely strong shaking belt that then propagated through northern Taiwan. This simulated characteristic has a good agreement with the known directivity phenomenon recorded by dense strong motion observations during the Chi-Chi earthquake. From the synthetic and observed waveforms along the profile, the source directivity effect can be observed even more clearly (Figure 8b). In the southern part, both synthetic and observed waveforms show a weaker amplitude but with higher frequency content. Conversely, the waveforms in the

northern stations are dominated by large amplitudes and long period phase as a result of strong directivity effect. This phenomenon can be found at most of the stations located in north Taiwan, such as TCU033 and TCU046 (Figure 8b). Part of the records in this profile have a larger discrepancy that may be because these stations are not exactly located on the profile but are 10 km distant. For example, the simulation results along the profile can not fit with the observed record at TCU031, but the synthetic waveform at TCU031 can explain the observation sufficiently (Figure 2b). In sum, the ground motion characteristics in a north-south direction, especially on the hanging wall, are dominated by strong slip patches and rupture directivity effects.

5. Conclusions

[25] With a three-dimensional realistic rupture source model for the Chelungpu fault that has excited the large M_w7.6 Chi-Chi earthquake and a three-dimensional Taiwan crustal model derived from a recent comprehensive travel-time tomography, we successfully reproduced the strong ground motions over a frequency band of 0.01–0.5 Hz. Comparison of the simulation results and observed waveforms clearly demonstrates that the heterogeneity of a three-dimensional velocity structure and the complex rupture process are two main factors affecting the PGV distribution and strong ground motion behavior. For the region close to the source rupture area, the PGV and ground motion are strongly influenced by the location of large asperities. An apparent rupture directivity effect propagating from south to north then has produced noticeable large PGV extending toward northern Taiwan. Low-velocity material under basins and the shallow part of the Coastal Plain generated significantly amplified ground motions. Because of the energy radiation property of the Chelungpu thrust fault, the seismic energy is mostly propagated along the downdip direction resulting in a weaker motion in the Central Range. Toward eastern Taiwan, the ground shaking is then amplified by a high velocity gradient under the Coastal Range. In general, the characteristics of nearby strong ground motion at different sites are principally dominated by intense source effects. This research indicates that the development of a valid method for the prediction of strong motion, as it is so hotly pursued in current seismological research, requires a detailed knowledge of the rupture source and a realistic three-dimensional crustal velocity model with a fine description of the near surface structure (basin and sedimentary plain). With efficient simulation codes and large computation facilities, a last requirement is a set of strong motion records with thorough coverage of a big earthquake such as the data set recovered by the TSMIP instruments during the Chi-Chi earthquake. With all these requirements, a careful validation analysis will establish our ability for strong motion prediction (over a practical frequency band) which is a central element in future earthquake hazard reduction.

[26] **Acknowledgments.** The authors would like to thank the Central Weather Bureau for providing TSMIP data used in this study. We also thank W.H.K. Lee and H.-C. Chiu for many clarifications about the data set. We deeply appreciate Ta-Liang Teng and J.-H. Wang for detailed and insightful reviews. Special thanks go to IESAS and the Seismological Lab at Caltech where many valuable discussions occurred. Much of this work was done while the author was a Ph.D. student at the Institute of Geophysics, National Central University. This research was supported by the Taiwan Earthquake Research Center (TEC) funded through National Science Council (NSC) with grant number NSC89-2921-M-008-012-EAF. The TEC contribution number for this article is 00003B.

References

Cerjan, C., D. Kosloff, R. Kosloff, and M. Reshef (1985), A nonreflecting boundary condition for discrete acoustic and elastic wave equations, *Geophysics*, *50*, 705–708.

Chang, W. F., and G. A. McMechan (1987), Elastic reverse-time migration, *Geophysics*, *52*, 1367–1375.

Chang, W. F., and G. A. McMechan (1989), Absorbing boundary conditions for 3-D acoustic and elastic finite-difference calculations, *Bull. Seismol. Soc. Am.*, *79*, 211–218.

Chang, W. F., and G. A. McMechan (1991), Wavefield extrapolation of body waves for 3-D imaging of earthquake sources, *Geophys. J. Int.*, *106*, 85–98.

Chang, W. F., and G. A. McMechan (1994), 3-D elastic prestack reverse-time depth migration, *Geophysics*, *59*, 597–609.

Chang, T. M., K. L. Wen, T. Furumura, and H. J. Chiang (2002), Surface wave excitation in the western coastal plain of Taiwan during the 1999 Chi-Chi earthquake, *J. Chin. Inst. Eng.*, *25*(4), 461–467.

Chen, H. W. (1996), Staggered-grid pseudospectral viscoacoustic wave field simulation in two-dimensional media, *J. Acoust. Soc. Am.*, *100*(1), 120–131.

Chen, C. H., W. H. Wang, and T. L. Teng (2001), 3D velocity structure around the source area of the 1999 Chi-Chi, Taiwan, Earthquake: Before and after the mainshock, *Bull. Seismol. Soc. Am.*, *91*, 1013–1027.

Cheng, W. B. (2000), Three-dimensional crustal structure around the source area of the 1999 Chi-Chi earthquake in Taiwan and its relation to the aftershock locations, *Terr. Atmos. Oceanic Sci.*, *11*, 643–660.

Clayton, R. W., and B. Engquist (1977), Absorbing boundary conditions for acoustic and elastic wave equations, *Bull. Seismol. Soc. Am.*, *6*, 1529–1540.

Furumura, T., and K. Koketsu (2000), Parallel 3-D simulation of ground motion for the 1995 Kobe earthquake: The component decomposition approach, *Pure Appl. Geophys.*, *157*, 1921–1927.

Furumura, T., and S. K. Singh (2002), Regional wave propagation from Mexican subduction zone earthquakes: The attenuation functions for interplate and inslab events, *Bull. Seismol. Soc. Am.*, *92*, 2110–2125.

Furumura, M., T. Furumura, and K. L. Wen (2001), Numerical simulation of Love wave generation in the Ilan basin, Taiwan, during the 1999 Chi-Chi earthquake, *Geophys. Res. Lett.*, *28*, 3385–3388.

Gropp, W., E. Lusk, N. Doss, and A. Skjellum (1996), A high-performance, portable implementation of the MPI message passing interface standard, *Parallel Comput.*, *22*(6), 789–828.

Hartzell, S. H., and T. H. Heaton (1983), Inversion of strong ground motion and teleseismic waveform data for the fault rupture history of the 1979 Imperial Valley, California earthquake, *Bull. Seismol. Soc. Am.*, *73*, 1553–1583.

Ho, M. Y., and T. C. Shin (1994), 3-D velocity structure of western Taiwan, *Meteorol. Bull.*, *40*, 216–234.

Ji, Chen, D. V. Helmberger, T.-R. Song, K.-F. Ma, and D. J. Wald (2001), Slip distribution and tectonic implication of the 1999 Chi-Chi, Taiwan, Earthquake, *Geophys. Res. Lett.*, *28*(23), 4379–4382.

Kagawa, T., S. Sawada, Y. Iwasaki, and A. Nanjo (1993), Modeling of deep sedimentary structure of the Osaka basin, *Proc. 22nd Earthquake Eng.*, 192–202.

Lee, K. S., and H. W. Chen (2000), Evaluate of the three-dimensional velocity structure in Taiwan region, in *Geophysical Annual Meeting, Taiwan*, 8, 97–102 (in Chinese).

Lee, S. J., and K. F. Ma (2000), Rupture process of the 1999 Chi-Chi, Taiwan, earthquake from the inversion of teleseismic data, *Terr. Atmos. Oceanic Sci.*, *11*, 591–608.

Lee, S. J., K. F. Ma, and H. W. Chen (2006a), Effect of fault geometry and slip style on near-fault static displacements caused by the 1999 Chi-Chi, Taiwan, Earthquake, *Earth Planet. Sci. Lett.*, *241*, 336–350.

Lee, S. J., K. F. Ma, and H. W. Chen (2006b), Three-dimensional dense strong motion waveform inversion for the rupture process of the 1999 Chi-Chi, Taiwan, earthquake, *J. Geophys. Res.*, *111*, B11308, doi:10.1029/2005JB004097.

Ma, K. F., J. H. Wang, and D. Zhao (1996), Three dimensional seismic velocity structure of the crust and uppermost mantle beneath Taiwan, *J. Phys. Earth*, *44*, 85–105.

Ma, K. F., J. Mori, S. J. Lee, and S. B. Yu (2001), Spatial and temporal distribution of slip for the 1999 Chi-Chi, Taiwan, Earthquake, *Bull. Seismol. Soc. Am.*, *91*, 1069–1087.

Rau, R. J., and F. T. Wu (1995), Tomographic imaging of lithospheric structures under Taiwan, *Earth Planet. Sci. Lett.*, *135*, 517–532.

Suppe, J. (1980a), A retrodeformable cross section of northern Taiwan, *Proc. Geol. Soc. China*, *23*, 46–55.

Suppe, J. (1980b), Imbricated structure of western foothills belt, south-central Taiwan, *Pet. Geol. Taiwan*, *17*, 1–16.

Wald, D. J., and T. H. Heaton (1994), Spatial and temporal distribution of slip for the 1992 Landers, California earthquake, *Bull. Seismol. Soc. Am.*, *84*, 668–691.

Wang, C. Y., C. H. Chang, and H. Y. Yen (2000), An interpretation of the 1999 Chi–Chi earthquake in Taiwan based on thin-skinned thrust model, *Terr. Atmos. Oceanic Sci.*, *11*, 609–630.

Wu, C., M. Takeo, and S. Ide (2001), Source process of the Chi-Chi Earthquake: A joint inversion of strong motion data and global positioning system data with a multifault model, *Bull. Seismol. Soc. Am.*, *91*, 1128–1143.

Yagi, Y., and M. Kikuchi (2000), Source rupture process of the Chi-Chi, Taiwan earthquake of determined by seismic wave and GPS, *Eos Trans. AGU*, *81*(22), s21A-05.

Yoshida, S., Koketsu, B. Shibazaki, T. Sagiya, T. Kato, and Y. Yoshida (1996), Joint inversion of near- and far-field waveforms and geodetic data for the rupture process of the 1995 Kobe earthquake, *J. Phys. Earth*, *44*, 437–454.

Zeng, Y., and C. H. Chen (2001), Fault rupture process of the 20 September 1999 Chi-Chi, Taiwan, Earthquake, *Bull. Seismol. Soc. Am.*, *91*, 1088–1098.

H.-W. Chen and K.-F. Ma, Institute of Geophysics, National Central University, Jung-Li 320, Taiwan. (hwchen@earth.ncu.edu.tw; fong@earth.ncu.edu.tw)

S.-J. Lee, Institute of Earth Sciences, Academia Sinica, Nankang, Taipei 115, Taiwan. (sjlee@earth.sinica.edu.tw)